Finite Element Studies of an Embryonic Cell Aggregate under Parallel Plate Compression

by

Tzu-Yao Yang

A thesis
presented to the University of Waterloo
in fulfillment of the
thesis requirement for the degree of
Master of Applied Science
in
Civil Engineering

Waterloo, Ontario, Canada, 2008

I hereby declare that I am the sole author of this thesis. This is a true copy of the thesis, including any required final revisions, as accepted by my examiners.

I understand that my thesis may be made electronically available to the public.

Tzu-Yao Yang

Abstract

Cell shape is important to understanding the mechanics of three-dimensional (3D) cell aggregates. When an aggregate of embryonic cells is compressed between parallel plates, the cell mass and the cells of which it is composed flatten. Over time, the cells typically move past one another and return to their original, spherical shapes, even during sustained compression, although the profile of the aggregate changes little once plate motion stops. Although the surface and interfacial tensions of cells have been attributed to driving these internal movements, measurements of these properties have largely eluded researchers.

Here, an existing 3D finite element model, designed specifically for the mechanics of cell-cell interactions, is enhanced so that it can be used to investigate aggregate compression. The formulation of that model is briefly presented and enhancements made to its rearrangement algorithms discussed.

Simulations run using the model show that the rounding of interior cells is governed by the ratio between the interfacial tension and cell viscosity, whereas the shape of cells in contact with the medium or the compression plates is dominated by their respective cell-medium or cell-plate surface tensions. The model also shows that as an aggregate compresses, its cells elongate more in the circumferential direction than the radial direction.

Since experimental data from compressed aggregates are anticipated to consist of confocal sections, geometric characterization methods are devised to quantify the anisotropy of cells and to relate cross sections to 3D properties. The average anisotropy of interior cells as found using radial cross sections corresponds more closely with the 3D properties of the cells than data from series of parallel sections.

A basis is presented for estimating cell-cell interfacial tensions from the cell shape histories they exhibit during the cell reshaping phase of an aggregate compression test.

Acknowledgments

I would like to express my sincere gratitude to my supervisor, Dr. G. Wayne Brodland. His inspiration and guidance during the time of this work, and his true passion in discovering knowledge have had and will have a remarkable influence in my professional career.

I wish to thank my family and friends for their support and belief in whatever path I choose in life.

This work would not have been possible without the untiring help of Jim Veldhuis in software and technical assistance.

Table of Contents

List of Figures

List of Tables

1 Introduction

Many fundamental biological processes, such as growth, differentiation, migration, and apoptosis, are mediated by changes in cell shape and cytoskeletal integrity (Watson 1991, Ingber, et al. 1995, Chen, et al. 2003). For example, anisotropies in cell shape affect the future positions of daughter cells and therefore are critical to cell fate (Théry, et al. 2005).

Cell shape is also important in the mechanics of three-dimensional (3D) cell aggregates as first revealed by centrifugation experiments of embryonic tissues (Phillips and Steinberg 1978). When spherical aggregates of isotropic cells are centrifuged, the cell masses and the cells of which they are composed flatten. Over time, as centrifugation continues, the cells anneal (spontaneously reshape and rearrange until individual cells are again nearly isotropic) even though the mass as a whole remains flattened. The same phenomenon is also observed in compression experiments of embryonic tissues between parallel plates (Phillips and Davis 1978, Foty, Pfleger, et al. 1996). Exhibiting a viscous-liquid behavior, the cells move past one another and resume their original, undistorted shapes. Comparable results from a two-dimensional (2D) finite element (FE) simulation of aggregate compression by parallel plates (Brodland 2003) are shown in Figure 1.1.
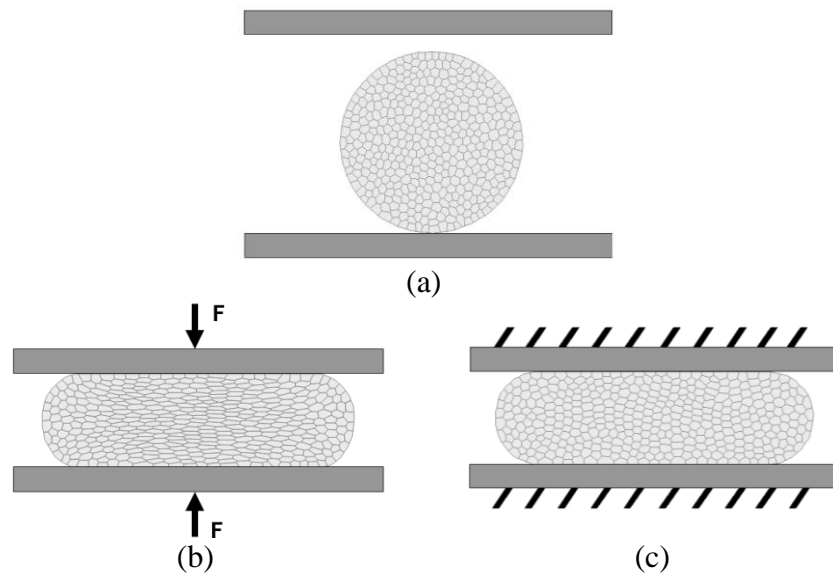
Figure 1.1: A parallel plate compression test of a 2D cell aggregate

1

A rapid compression causes the cell mass and individual cells to flatten normal to the parallel plates (Figure 1.1b) while the rounding and relative moments of cells eventually produce an annealed state (Figure 1.1c).

The present study simulates the same compression experiment with a 3D FE model. The reason for including the third dimension is because even though 2D simulations elucidate important concepts in cell mechanics, they are unable to capture certain cell phenomena that are demonstrated in 3D simulations (Brodland, Yang and Veldhuis 2008). Disparities in a 2D model are due to its reduced dimension, which produces limited cell connectivity and fewer numbers of cell neighbours when compared to a 3D model. For example, a 3D model can accurately describe the connectedness of cells, whereas a 2D model, as represented by the cutting plane, portrays the cells as isolated groups (Figure 1.2). In addition, a 3D cell is typically surrounded by an average of 14.3 neighbours and a 2D cell only has on average 6.3 neighbours.
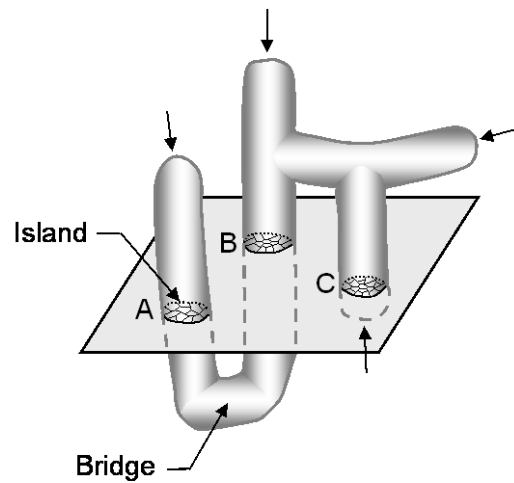
Figure 1.2: Fundamental difference between 2D and 3D models

Dimension-dependent instabilities can also arise as a chain of cells breaks in 3D but remains contiguous in 2D. Dimensionality differences are also evident in other physical phenomena such as wave propagation (Olsen, Nigbor and Konno 2000).

To capture the movement of embryonic cells, we assume a γ-μ model where a constant interface type-specific tension γ is acting on each cell boundary and a viscosity μ

represents the mechanical effect of the cytoplasm. Taking into account μ, which other models do not do, allows the time course of cell motions to be predicted.

According to the *differential adhesion hypothesis*, cell type-specific adhesions drive the liquid-like behaviour of embryonic tissues during morphogenesis (Foty, Forgacs, et al. 1994, Foty and Steinberg 2005). They guide the assembly of cells and tissues into anatomically "correct" higher level structures (Steinberg 1993), which represent an equilibrium configuration where the interfacial free energy of the system is minimized (Foty, Forgacs, et al. 1994).

For cell aggregates, there are two types of tensions. Showing a single, exterior cell in aggregate, Figure 1.3 defines the tension acting at the cell-medium boundary as *surface tension* and the tension acting at the cell-cell interface as *interfacial tension*.
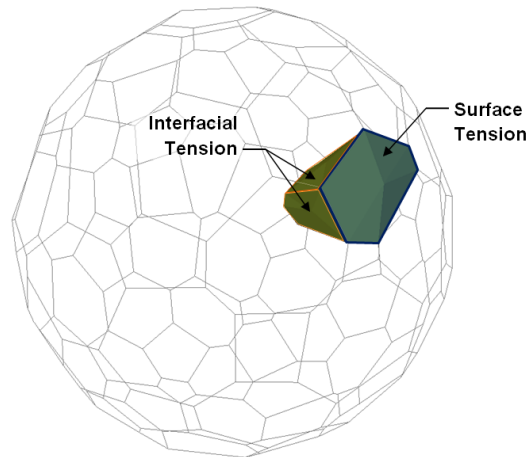
Figure 1.3: Surface and interfacial tensions for a cell aggregate

The magnitudes of surface and interfacial tensions strongly depend on the state of the cellular cytoskeleton (Forgacs 1998, Gov, Zilman and Safran 2003, Fournier, Lacoste and Raphael 2004), which is a dynamic network of protein fibres (Figure 1.4). There are three types of protein fibers: microtubules, microfilaments, and intermediate filaments. Microtubules, which dynamically assemble and disassemble, act as a local scaffold and are the thickest in diameter. Microfilaments are contractile and a prime source of the cell surface tensions, while intermediate filaments stabilize the cytoplasm and the structures it contains (Alberts, et al. 2004).

3
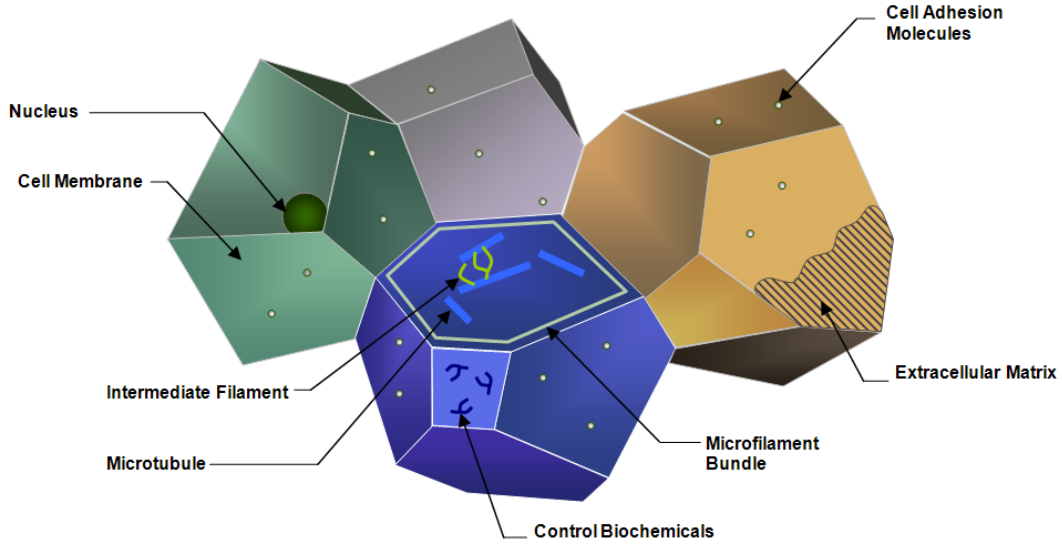
Figure 1.4: A typical biological cell aggregate

Interactions between these cytoskeletal components generate tensions at the cell-medium and cell-cell interfaces. Tension values are also correlated with the contraction of the cell membrane and the number and binding strength of cell adhesion molecules (Beysens, Forgacs and Glazier 2000). Collectively, the equivalent surface or interfacial tension γ_{AB} can be calculated as:

$$\gamma_{AB} = F_A^{Cyto} + F_B^{Cyto} + F_A^{Mem} + F_B^{Mem} - F_{AB}^{Adh} + F_{AB}^{Other} \qquad \text{Eq. 1.1}$$

where F_A^{Cyto} is the combined force from the cytoskeletal components, F_A^{Mem} is the cell membrane force, F_{AB}^{Adh} is the adhesion forces, and F_{AB}^{Other} is any other force acting on the cell interface (Brodland 2002). The subscripts A, B, and AB designate the corresponding cell(s) that produce the force.

Using a FE model overcomes two challenges typically associated with laboratory experiments. The first issue arises from the fact that accurate measurements of mechanical properties are difficult to achieve in the laboratory. Surface tensions, while easy to allude to, are far from easy to quantify in live, irregularly shaped cells (Morris and Homann 2001). To date, no one has been able to measure the bulk interfacial tension between cells via compression experiments or any other experiments. The second issue is the delicate nature of biological cells which significantly complicates physical

4

measurements of cell shape. Cell shape data usually have to be inferred from planar images.

With FE simulations, geometric data are readily available for analysis and the changes in individual cell shape under the influence of different surface and interfacial tensions can be determined. Also, surface and interfacial tensions can be specified at will.

This study theoretically analyzes the relationship between cell shape history and interfacial tensions using principles of mechanics, and then verifies the theoretical predictions using FE results. This study also aims to provide a way for expediting the extraction of 3D cell shape data in real experiments from planar images.

Based on the preceding discussion, the goal of the present study is to simulate the parallel plate compression of embryonic cell aggregates with the FE method and use the results to: (1) investigate the effects of surface and interfacial tensions on cell shape history, (2) develop an equation that relates cell shape history and the interfacial tension, (3) provide validation for theoretical shape analyses that can be used to interpret other numerical or experimental observations, and (4) determine if there exists a correlation between the 2D sections and 3D cell shape.

Collectively, these objectives will provide insights into factors that determine cell shape history, and lead to a method that will finally make it possible to extract the interfacial tensions of cells in aggregate.

2 Literature Review

This chapter reviews previous cell aggregate compression experiments and previous 3D models for the mechanics of cell-cell interactions. The available computational approaches for 2D models, with their strengths and weaknesses, have been discussed by Brodland (2004).

2.1 Cell Compression Experiments

The mechanics of cell-cell interfaces has been studied using a wide range of experimental techniques that can be divided into two groups: (1) techniques for global loading of individual cells, such as microplate manipulation (Thoumine and Ott 1997), micromanipulation (Zhang, et al. 1991), or whole cell micropipette aspiration (Evans and Yeung 1989), and (2) techniques aiming at local loading of cells, e.g., atomic force microscopy (Mathur, et al. 2001), cell poking (Petersen, McConnaughey and Elson 1982), bead micromanipulation (Bausch, Ziemann, et al. 1998), or partial cell aspiration with micropipettes (Sato, et al. 1990).

Specific to the present study, the following section reviews the experiments that have been developed to investigate the response of aggregated cells when become compressed.

Phillips and Steinberg (1969) devised a modification of the sessile drop method to test the adhesive properties of embryonic cells. In this method the cells flatten under prolonged centrifugal forces, while the intercellular adhesiveness in aggregates provides the resistance to deformation and the drive to round up. As the final geometry of the aggregate only partly reflects the strengths of the intercellular adhesion, other possible effects of centrifugation are also accounted for in their calculations. These effects include the centrifugal acceleration, buoyant densities of the aggregates, and the adhesive interactions of the aggregates with the agar substratum.

Phillips and Davis (1978) described two physical tests for liquid-tissue morphogenesis in cell aggregates. In one test, spherical cell aggregates in culture medium are deformed by

6

being compressed between parallel glass cover slips. The flattened embryonic cells exhibit viscous-liquid behaviors by returning to their original rounded shapes. This annealing process involves self-propelled translocations or passive slippage movements or both. Devised to measure surface tensions, the other test has one compressing glass mounted on the end of a flexible quartz fiber (Figure 2.1).
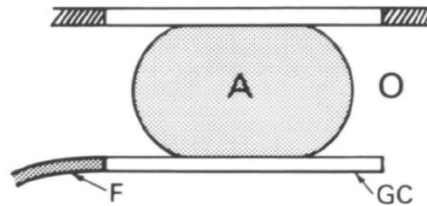
**Figure 2.1: An aggregate compressed between two glass chips, one of which is glued to a
quartz fibre (F)**

The degree of bending in the fiber can be used to calculate the forces exerted by the cell aggregate. Once the internal cell deformation within a compressed aggregate has been dissipated by cell slippage, its surface tension is the sole force resisting deformation (Phillips and Davis 1978).

Foty et al. (1994) introduced a thermostated parallel plate compression apparatus (Figure 2.2) specifically developed to measure the surface tension of living embryonic cells.
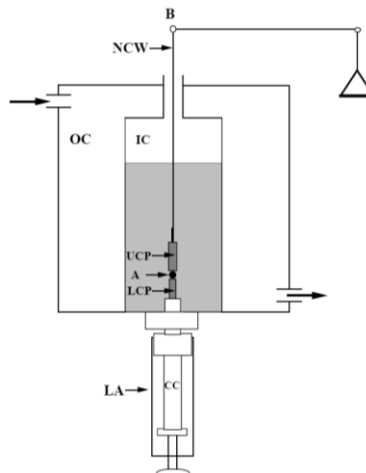
Figure 2.2: The parallel plate compression apparatus

7

The temperature in the inner chamber (IC) is maintained by a thermostated circulating water pump. The upper compression plate (UCP) is suspended from the balance arm (B) by a nickel-chromium wire (NCW). The compression of the aggregate reduces the load measured by the balance by an amount equal to the force acting upon the cell aggregate (Foty, Forgacs, et al. 1994)

2.2   Previous Three-Dimensional Models

The spatiotemporal dynamics of biological cells can sometimes be well described by a simple theoretical model. Perhaps one of the greatest advantages is the ability to test hypothesis in *in silico* experiments, thereby eliminating unnecessary laboratory experiments that are often expensive and time consuming. In addition, computational modelling also allows for the extraction of mechanical properties of living cells from numerical simulations by comparison to experimental results. Furthermore, a validated theoretical model can be used to interpret or predict other experimental observations.

2.2.1   Centric Models

In centric models the cells are represented by individually interacting objects. These models are computationally intense, as every single cell is included in the simulations; however, this method also allows for the interaction rules to be chosen intuitively from experimental observations.

Palsson (2001) proposed a centric model for simulating, in three dimensions, individual biological cell movements in multicellular systems. With the model, he investigated cell aggregation, embryogenesis, limb formation, and wound healing. In the Palsson model each cell is idealized as a deformable ellipsoid with individually chosen properties and constant volume. In addition, the viscoelastic properties of the cell are incorporated as a nonlinear spring in parallel with a spring and dashpot in series (Figure 2.3) contained in each axis of the ellipsoid.
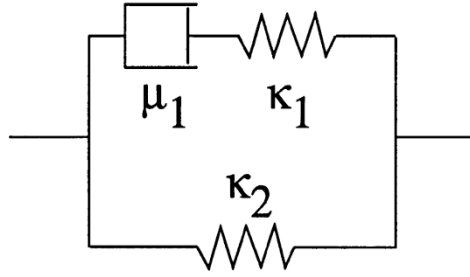
Figure 2.3: The combination of springs and dashpot used to model cell viscosity

The values of μ_1, κ_1, and κ_2 in each spring-dashpot system are calculated based on the lengths of the three axes.

A cell experiences three types of forces: active, passive, and a viscous drag force. Generated in response to chemotactic signals, the active force moves the whole cell along its anterior-posterior axis towards the signals. The magnitude of this force is set to a constant value of 5 x 10^{-3} dyn whenever the chemical concentration exceeds a threshold. The passive forces arise from the adhesive and elastic interactions with surrounding cells, and are determined based on the proximity *d* of the cells to one another and their relative axis orientations (Figure 2.4).
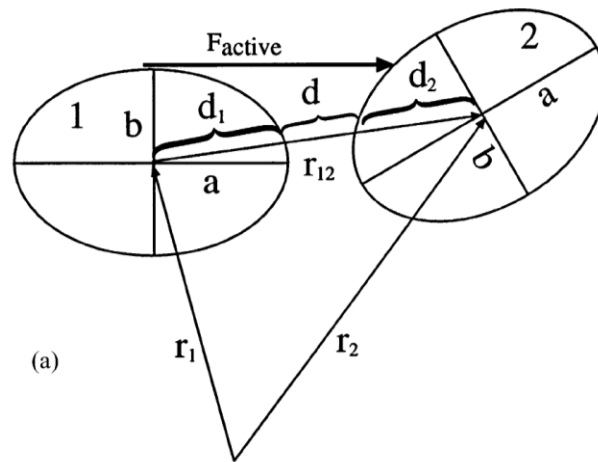
Figure 2.4: The distance between the surfaces of two cells is determined

The active and passive forces are balanced by the drag force, which is generated from the cell movements through a viscous environment. The equilibrium state in the Palsson model has *d* < 0 such that a space filling configuration may be created (Figure 2.5).

9
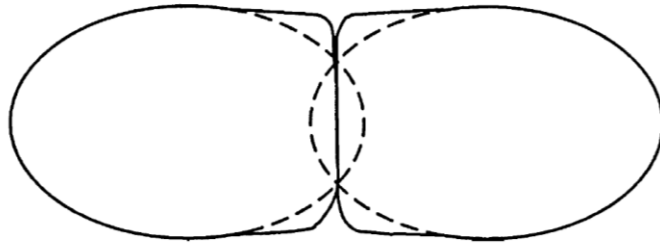
Figure 2.5: The distance between cells is negative to create a space filling configuration

With this model, Palsson was able to adequately simulate the behaviour of embryonic tissues under parallel plate compression (Figure 2.6). The calculated values for surface tension and the adhesion constant were within the biological values.
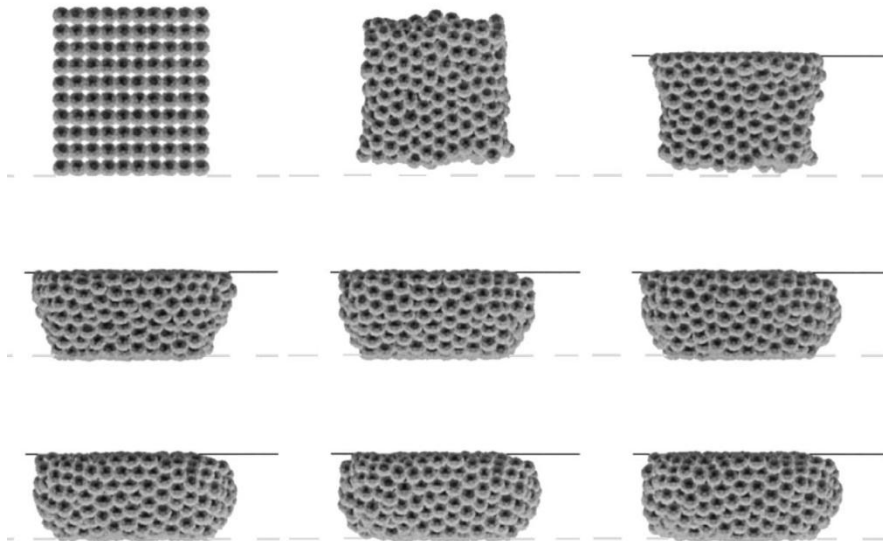
Figure 2.6: Parallel plate compression of a cell aggregate through time

Also demonstrated in several sorting simulations, this model offers the ease of motion between individual cells. However, the method for generating forces and the stiffness of cells may not accurately represent the actual physical system. In addition, the Palsson model is not truly space filling as in the case of real biological aggregates. Furthermore, the cells are restricted to one special cell form, which does not allow for more variations in cell shape and size.

Clem, Konig, and Rigaut (1997) developed a centric model to investigate the renewal of the nasal epithelium. In this model the cells are represented by ellipsoids with random

orientation, size, and shape deviations. The cells are capable of growth and division to simulate the evolution of cell cycle. During a cell division, the daughter cell F which does not take the place of the mother cell M is displaced in the direction towards the largest empty adjacent space available (Figure 2.7).
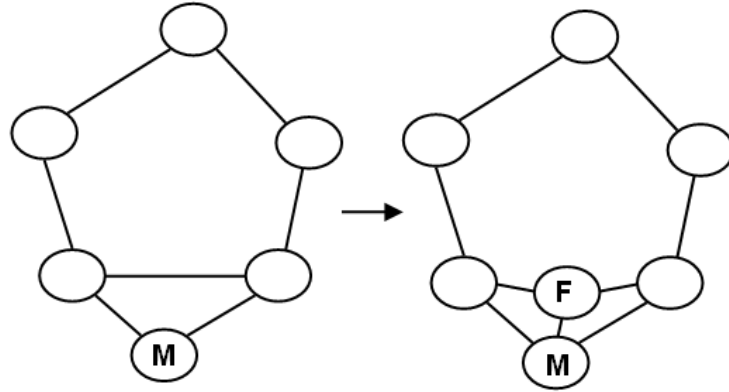
Figure 2.7: Stem cell M undergoes mitosis in which daughter cell F moves into the largest empty adjacent space

This displacing movement continues until the overlapping of the daughter cells ceases. In addition, when a collision with the neighbouring cells is imminent, the neighbours move in accordance with vector equations. This model has the ability to simulate the ease of cell motion, but lacks the complexity required to replicate forces and time accurately.

Schaller and Mayer-Hermann (2005) also developed a centric model to study the morphology and growth of tumour cells. Similar to the Palsson model, this model represents the cells as deformable spheres with dynamic radii. The absolute value of the elastic force between two spheres is a function of the maximum overlap h_{ij} (Figure 2.8) and the elastic properties of the spheres. The cells also experience intercellular adhesion forces calculated based on the contact area A_{ij} and the chemical concentrations of the spheres.
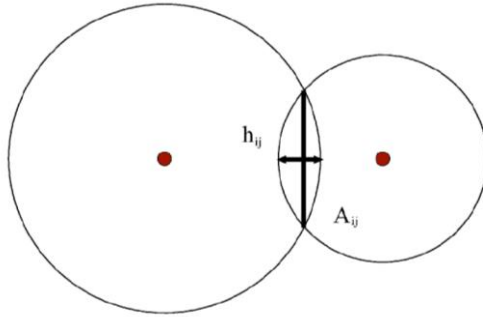
Figure 2.8: 2D illustration of overlapping spheres

In dense tissues where many spheres overlap (Figure 2.9), the Voronoi contact surface, marked with a bold line, is used to provide a more realistic estimate of the cellular contact area A_{ij}.
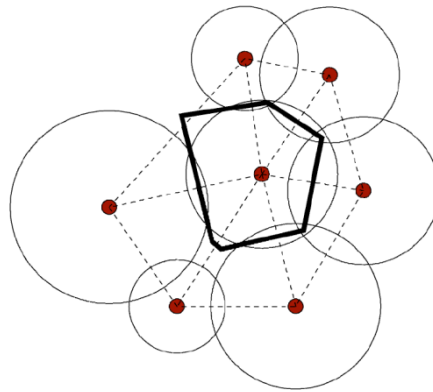
Figure 2.9: Voronoi contact surfaces are used in dense tissues

In addition to the elastic and adhesive forces, the equations of motion also consider possible random forces, cell-medium friction, and cell-cell friction. These cells are able to grow, divide, and die to represent the actual population dynamics of cells. Experimental growth curves and typical tissue morphology were reproduced well in simulations. However, in reality this model may not be adequate for cells as the mechanics of the cytoskeleton cannot be well described by purely elastic responses. There also exists an issue of accuracy in the method of determining the contact surfaces, which directly affects the force calculations. In addition, the space filling nature of real-life cells is not replicated in this model.

2.2.2 Boundary Vertex Models

In boundary vertex models each cell is represented by a list of vertices that define the occupied space. Accordingly, the cells are polyhedral in shape. The interaction rules in these models are formulated to minimize the boundary lengths or contact surface areas.

The first boundary vertex model was formulated by Fuchizaki et al. (1995) to study grain growth in metals. In their model, triangulation is performed for each polygonal face around a center node (Figure 2.10), which allows the face to deform in a non-coplanar fashion.
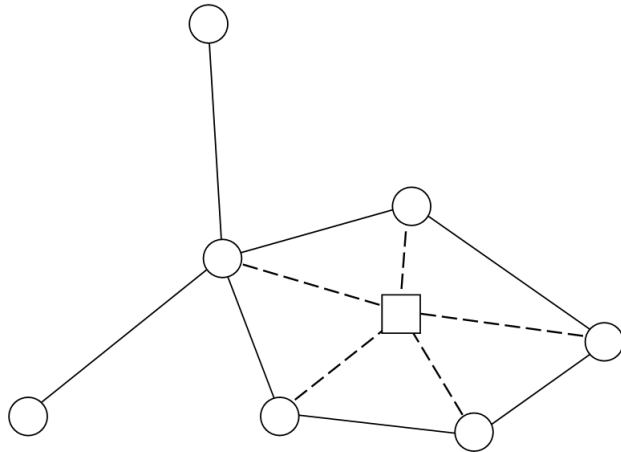
Figure 2.10: Triangulation of a polygonal face

The relevance of this model arises from the fact that biological cell movements are also driven by interfacial tensions. The equations of motion are derived to minimize the free energy of the cell boundary and the Rayleigh dissipation function associated with the cell boundary motion. However, a system may lock in a local minimum instead of a global minimum.

Additionally, this model is equipped with an algorithm to deal with the entanglements of edges. When an edge becomes shorter than a specified length Δ, the model executes a recombination process (Figure 2.11), in which the system loses (gains) a triangular face during the left to the right (the right to the left) reaction.
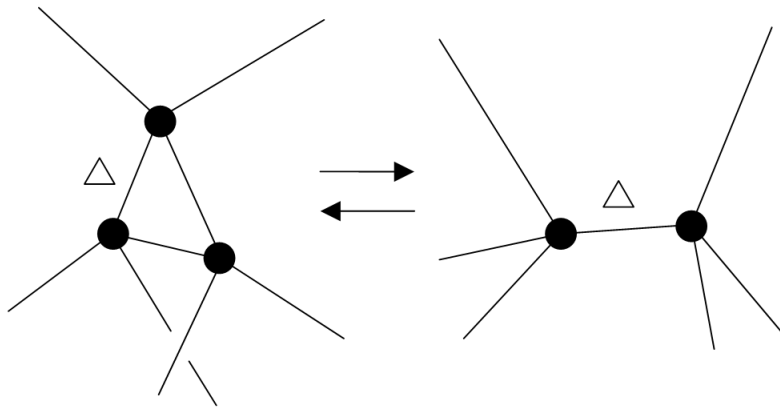
Figure 2.11: A recombination algorithm

This rearrangement algorithm greatly increases the ability for the cells to move and relocate within the aggregate (Fuchizaki, Kusaba and Kawasaki 1995).

Honda et al. (2004) developed a 3D cell model of a multicellular aggregate to investigate the deformation and rearrangement of eukaryotic cells under the influence of external forces. The cells are convex polyhedra, without gaps or overlaps, generated using a Voronoi subroutine. The vertex motions lead toward minimization of the total free energy of the system, which includes the surface and interfacial energies of the cells and the energy of cell compression and expansion. The same cell rearrangement algorithm as the Fuchizaki model is utilized in this model, and is illustrated by faces in Figure 2.12.
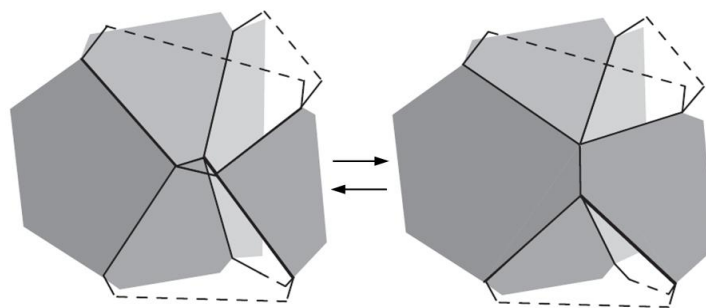
Figure 2.12: Reconnection of neighbouring vertices in a 3D tessellation consisting of faces

Honda et al. demonstrated the ability of the model to reproduce the behaviour of cell aggregates under centrifugal flattening. The deformed cells show annealing and relative cell movements (Figure 2.13), which are observed in laboratory experiments.

14
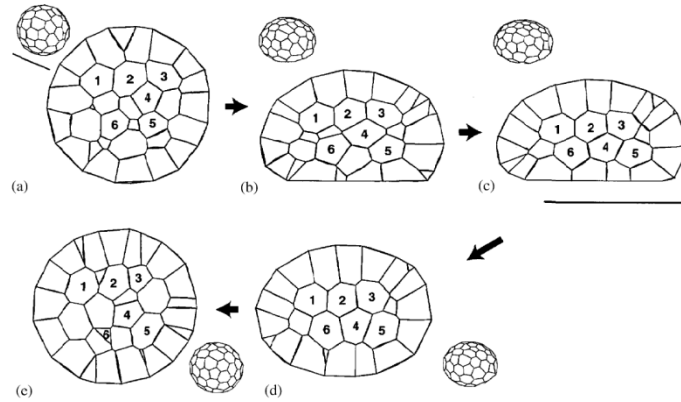
Figure 2.13: Sections through a cell aggregate during application and removal of centrifugal forces

Although the cell geometries can be adequately replicated, the model cannot predict time scales or forces associated with the deformation of the cytoplasm. This drawback is due to the lack of physical μ representing cell viscosity. Furthermore, the cell interfaces are forced to remain flat, which is a geometric restriction that may influence the cell shapes.

Having reviewed the above, we conclude that to properly model biological cells in three dimensions, a computational model should: (1) be truly three dimensional, (2) capture the close-packed geometry of real cell aggregates, (3) calculate the forces due to interfacial tensions correctly, and (4) account for the viscous forces generated by the deformation of the cytoplasm based on current cell geometry (Viens and Brodland 2007). Specifically developed to satisfy all of the above requirements, the finite element model used in this study is discussed in Section 3.

3 The Finite Element Model

The 3D finite element model used in this study satisfies the criteria for modelling biological cells as outlined in Section 2.2. This chapter briefly describes this model, and the enhancements made to a previous cell rearrangement algorithm (Viens and Brodland 2007). Lastly, the procedure for simulating the parallel plate compression experiment is described in Section 3.5.

3.1 The Finite Element Mesh

To generate a 3D mesh that is representative of real embryonic aggregates, two important features of cell masses must be captured: the forces they generate and their close-packed structure.

Homogenous cell aggregates form into a spherical droplet to minimize the surface area. For an aggregate of a large number of cells, the outer surface of the cell mass will tend to be spherical and the interior will be hexagonal closed-packed (Goel and Doggenweiler 1986). Accordingly, each embryonic cell is modeled by a closed-packing convex polyhedron generated randomly via Voronoi tessellation (Figure 1.4). The Voronoi mesh generation is performed by NalaProcess, which is a custom software package written in the Civil Engineering Biomechanics Laboratory at the University of Waterloo. The program is specifically designed to create and alter Voronoi tessellations for use in FE simulations.

In addition, we assume geometric restrictions, which are applied during the mesh generation: (1) two cells meet at one face, (2) three faces meet at one edge, and (3) four edges meet at one vertex. These geometric relations are better visualized in Figure 3.1a showing four interior cells within a typical Voronoi tessellation.

<center>(a)   (b)</center>
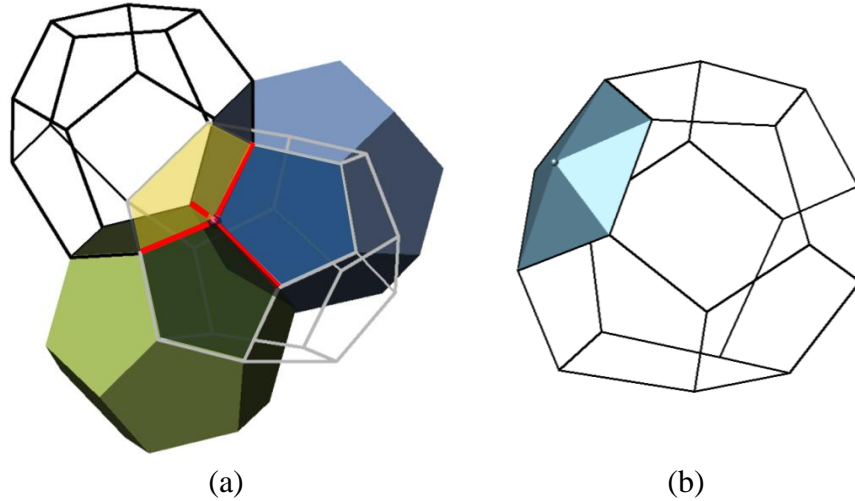
Figure 3.1: Typical Voronoi tessellation. (a) four interior cells (b) triangulated surface

Each vertex is connected to 4 edges, 6 faces, and 4 cells; each edge is connected to 3 faces, 3 cells, and 2 vertices; each face is connected to 2 cells, *p* vertices, and *p* edges; and each cell is connected to *f* faces, *fp*/**3** vertices, and *fp*/**2** edges. Each face is also subdivided by revolving around its centroid node (Figure 3.1b). This triangulation provides the freedom for faces to become convex or concave and the ability for cells to balance pressure differences.

3.2 Calculation of Cytoplasm Stiffness Matrix and Nodal Forces

As in other recent cell models (Bodenstein 1986, Chen and Brodland 2000, Graner and Glazier 1992, Honda, Tanemura and Nagai 2004, Umeda and Inouye 2004), the mechanical effects of the cytoplasm and organelles of the cell (Figure 1.4) are incorporated and respectively modeled as an incompressible viscous fluid of viscosity μ, and cell type-specific tensions γ acting on the cell surface (Viens and Brodland 2007).

3.2.1 Cytoplasm Stiffness as Viscous Fluid of Viscosity μ

As real cells experience strain rates of merely a few tens of percent per hour, the cytoplasm and the organelles of the cell can be modeled as a viscous fluid (Clausi and Brodland 1993). The cytoplasm becomes viscoelastic at much higher strain rates (Bausch, Moller and Sackmann 1999). In this model, the viscous effects of the cell cytoplasm are achieved through sets of three orthogonal dashpots whose axes correspond

<center>17</center>

with the principal axes of the cell they model (Viens and Brodland 2007). Figure 3.2 illustrates a set of orthogonal dashpots in one direction.
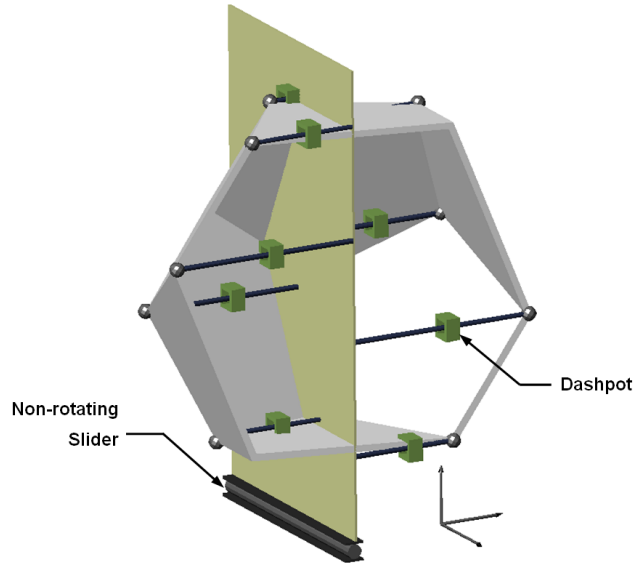
Figure 3.2: System of orthogonal dashpots in the x-direction

The stiffness of the dashpots is calculated as follows:

$$\mu_A = \frac{g\mu BC}{nA}$$ Eq. 3.1

where $\boldsymbol{g}$ is a form factor of 35.36, $\boldsymbol{\mu}$ is the cell viscosity, $\boldsymbol{n}$ is the number of nodes that comprise the cell, and $\boldsymbol{A}$, $\boldsymbol{B}$, and $\boldsymbol{C}$ are the respective lengths of the major axes of the cell (Brodland, Viens and Veldhuis 2007). A series of 3D validation tests show that the dashpot system adequately captures both tension and shear in isotropic cells, and the compression characteristics of anisotropic cells (Viens and Brodland 2007). Tetrahedra elements are not used here to model the cytoplasm, because they cause a spurious stiffening effect and interfere with proper neighbour changing (Brodland, Viens and Veldhuis 2007).

3.2.2 Nodal Forces Produced by Cell Type-Specific Tensions γ

Having discussed how type-specific tensions γ on cell interfaces arise in Chapter 1, this section describes the implementation of γ as nodal forces in the FE model. The effect of

18

γ is modeled by triangular surface elements that cover the cell surface, each with nodal forces acting as specified in Figure 3.3 .
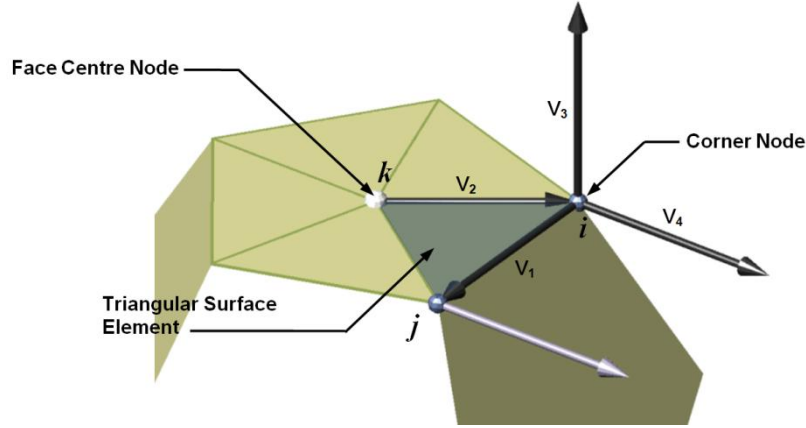
Figure 3.3: Set of vectors used in determining force direction, for a specific triangular sub-face and edge, ij

Each triangular surface element has one face centre node k and two corner nodes i and j. The following paragraphs describe the method used to calculate the equivalent nodal forces that represent the tensions acting along edge ij in Figure 3.3. First, a vector V_1 is formed from corner node i to corner node j, and a vector V_2 is formed from the face centre node k to corner node i. Subsequently, a normal to the surface triangle is calculated by the cross product of V_1 and V_2, as represented by V_3:

$$V_3 = V_1 \times V_2$$

Eq. 3.2

Lastly, a vector V_4 in the plane of the surface triangle and normal to edge ij is constructed as follows:

$$V_4 = V_3 \times V_1$$

Eq. 3.3

The tension γ associated with edge ij is assumed to generate two equivalent nodal forces, each with a magnitude equal to γ times half of the length of edge ij. The two forces act in the direction of V_4 at node i and node j, respectively.

The above procedure is repeated for each side of the triangular surface elements. Accordingly, the face centre node of an n-sided polygonal face experiences a net force of

19

2n force vectors. Each corner node experiences two force vectors from each of the 12 triangular sub-faces (refer to Figure 3.1a) that join at the node for a total of 24 vector forces. The motions of the cell aggregates are driven by this set of equivalent nodal forces.

3.3 Governing Equations

In the finite element method, the force-displacement relationship is described by the equation:

$$C\dot{u} + Ku = f$$

Eq. 3.4

where C is the damping matrix of the system, K is the stiffness matrix of the system, f is the applied force vector, u is the nodal displacement vector, and $\dot{u}$ is a displacement derivative with respect to time, or the velocity vector. In a viscous system, the stiffness matrix K can be set to zero. By using a forward difference scheme, Eq. 3.4 is rewritten as follows:

$$C\dot{u} \cong C\frac{\Delta u}{\Delta t} = \frac{1}{\Delta t}C\Delta u = f$$

Eq. 3.5

$$\frac{1}{\Delta t}C\left(u_{q+1} - u_q\right) = f_q$$

Eq. 3.6

where the subscript denotes a specific time step, Δu is an incremental displacement, and Δt is an incremental time step. In addition, a volume constraint is imposed on each cell using a Lagrange side condition as very soft tissues are often assumed to be incompressible (Miller 2005).

3.4 Cell Rearrangement Algorithms

The finite element model includes a cell rearrangement algorithm, which is invoked when an edge becomes shorter than a specified length. A cell rearrangement algorithm is necessary, because a shortening edge eventually becomes inverted and produces an invalid geometry where the two cells connected by the short edge overlap. Whether a

20

short edge signals the cohering or the separating of neighbouring cells depends on the geometry of the three faces connected to it.

Figure 3.4 shows four types of initial geometries based on the number of triangular faces associated with the short edge. The short edge is highlighted in red.

(a) Case 1 (previous): All faces have more than three edges

(b) Case 2 (previous): One face with three edges and two with more than three edges

(c) Case 3 (new): Two faces with three edges and one with more than three edges

(d) Case 4 (not yet observed): All faces have three edges
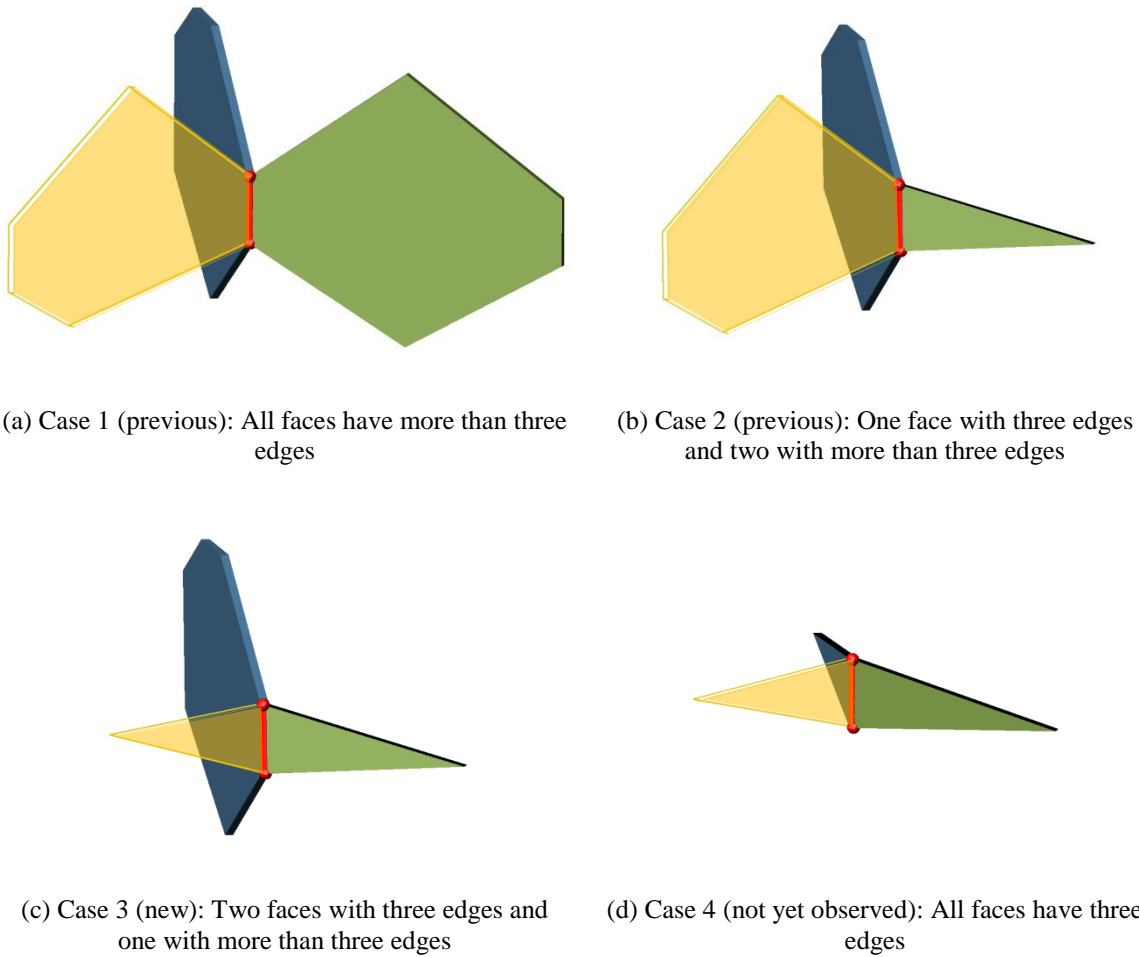
Figure 3.4: Four types of initial geometries

The previous model (Viens and Brodland 2007) was capable of handling the Case 1 and Case 2 initial geometries, as described in Section 3.4.1 and Section 3.4.2, respectively. The Case 3 cell rearrangement is developed by the present study in Section 3.4.4 while a possible algorithm is proposed for the Case 4 initial geometry in Section 3.4.5.

21

3.4.1 Case 1 Cell Rearrangement

In the first scenario (Case 1) where all faces have more than three edges (Figure 3.4a), a shortening edge signals the progression of two non-neighbouring cells moving closer to one another. As a result, the mesh is geometrically altered to allow these two cells to contact through a newly created face. Figure 3.5 schematically demonstrates the details of this cell rearrangement.

(a) 1 edge and 2 nodes are deleted

(b) 3 faces lose an edge

(c) 6 edges get re-noded

(d) 6 faces gain an edge

(e) 3 nodes, 3 edges, and 1 face are created
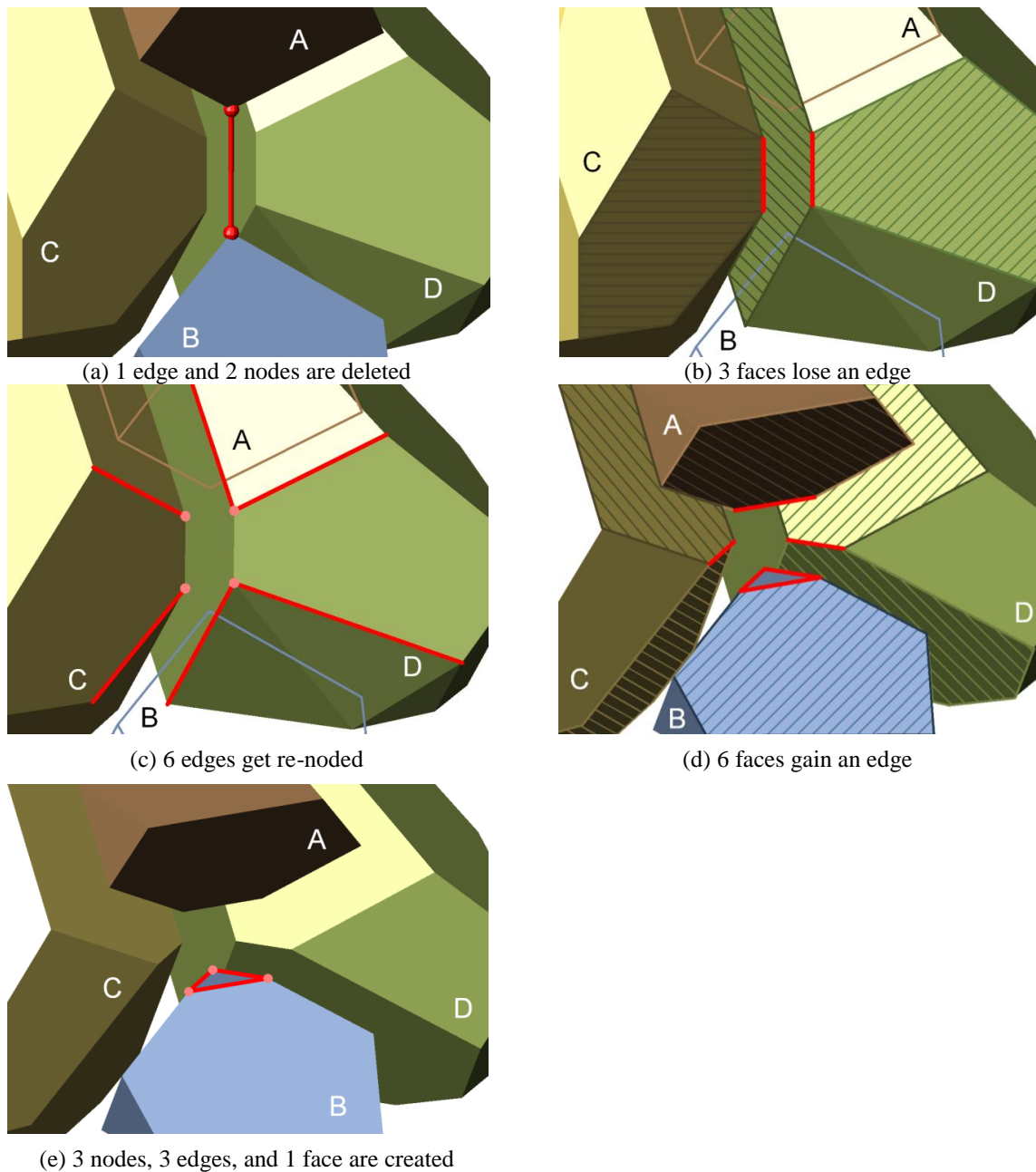
Figure 3.5: Case 1 cell rearrangement

In Figure 3.5a, non-neighbouring cells *A* and *B* are initially separated by a short edge along the triple junction between cells *C*, *D*, and *E* (removed to reveal the short edge). As cells *A* and *B* continue to move closer together, the shortening edge is deleted and a small triangular face is created in the last step to allow contact. Meanwhile, several intermediate adjustments are made to ensure the geometric conformance of the five cells involved, as listed in the above figure captions.

Note that these geometric adjustments result in the removal of an edge from each of the three faces (Figure 3.5b) surrounding the deleted short edge. For instance, one can follow the outward-facing green face of cell *D* transforming from a pentagon to a quadrilateral. Issues arise for triangular connected faces where a reduction in the edge count renders a meaningless topology. Therefore, the Case 1 rearrangement can only be sensibly executed for initial geometries, in which all connected faces have more than three edges.

3.4.2   Case 2 Cell Rearrangement

Figure 3.4b defines the Case 2 initial geometry where the short edge is part of one triangular face. In Case 2, a shortening edge essentially prompts an inverse Case 1 operation. Imagine a rotation of $90°$ so the single triangular face in Figure 3.4b is flat and perpendicular to the page. This rotated geometry can be viewed as the final step of Case 1 (Figure 3.5e). A shortening edge indicates a shrinking triangular face or a diminishing contact between two retreating cells. Therefore, the parting of two contacting cells is required. This disjoining of cells is achieved by performing Case 1 in a reversed order. In contrast with Case 1, the shrinking triangular face is ultimately replaced by a new edge that separates the two cells in question.

3.4.3   Motivation for the Case 3 Cell Rearrangement

Figure 3.4 also shows the remaining two possible initial geometries: Case 3 (two triangular faces) and Case 4 (three triangular faces). The occurrences of these two cases were assumed by the previous model to be extremely rare. This assumption is quite reasonable considering the geometric restrictions imposed on the meshes. Therefore, no

23

algorithm for their associated neighbour change was implemented. A similar cell rearrangement model was first used by Fuchizaki, Kusaba and Kawasaki (1995).

Offering two cases of cell rearrangement, the previous algorithm is adequately robust such that large deformation of a cell aggregate can be simulated without significant residual strains. However, our simulations showed that undesirable configurations occur regularly within larger meshes, which naturally contain more atypical geometries, or during longer simulations when many neighbour changes have taken place. This result is due to the fact that cell rearrangements are only executed for the initial geometries of Case 1 and Case 2, while those of Case 3 (Figure 3.4c), which do occur sporadically, are assumed improbable and bypassed. The Case 4 initial geometries (Figure 3.4d) may be treated as invalid without consequences for they have not been observed in actual Voronoi meshes.

Figure 3.6 shows the evolution of a Case 3 initial geometry into a distorted cell. Note that for clarity the surrounding cells are not displayed. Circumvented by the previous algorithm, the Case 3 initial geometry has a short edge (highlighted in red) that is part of two triangular faces (Figure 3.6b). Figure 3.6c to Figure 3.6e show the formation of a "spike" as the necessary detachment of the yellow cell is left unperformed. This "spike" subsequently obstructs the upward movement of the purple cell underneath (see Figure 3.6f to Figure 3.6h).

In Figure 3.6, we also observe an inconsistency in the mesh and its geometric assumptions. Recall that two neighbouring cells are expected to contact at a single face. However, the illustrated purple cell and a top cell (removed in figures) are actually connected via two faces (Figure 3.6f). This geometric exception is why Case 3 does occur infrequently in larger meshes.

(a)

(b)

(c)

(d)

(e)

(f)

(g)

(h)
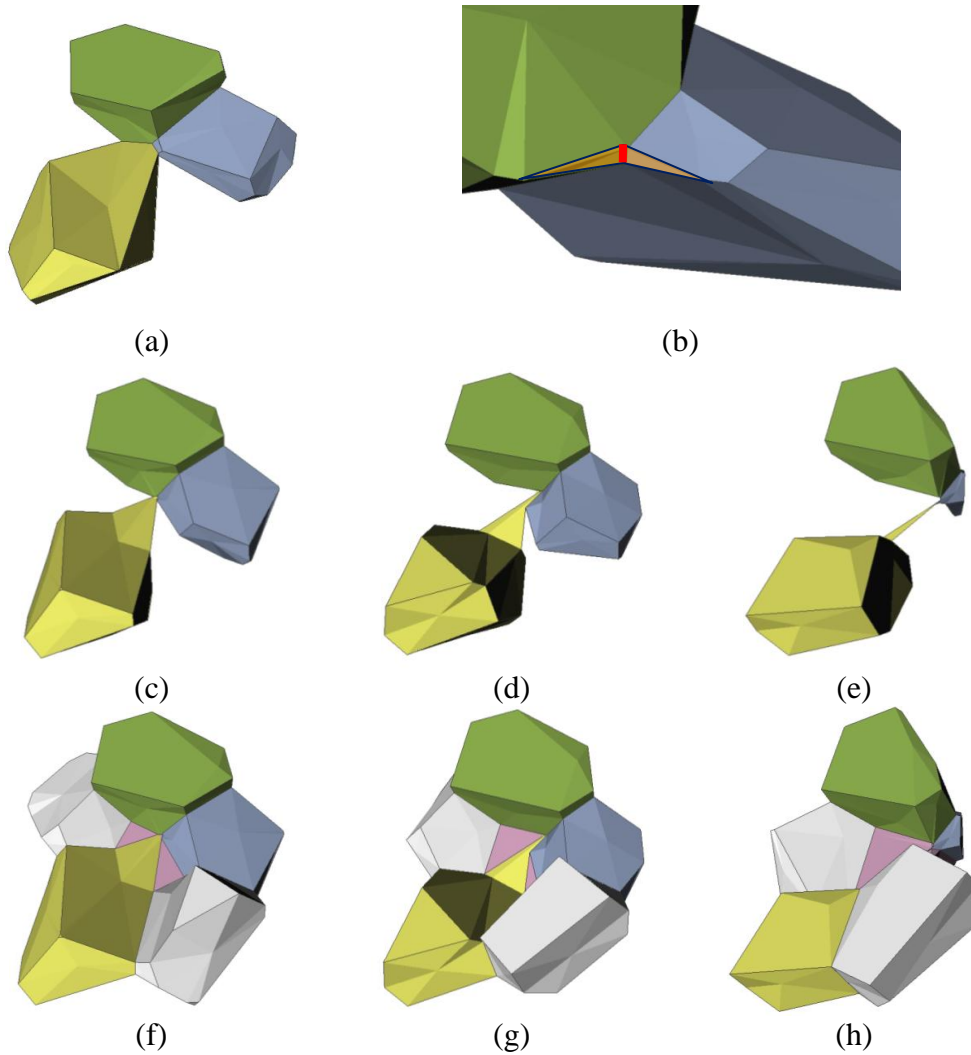
Figure 3.6: Evolution of a Case 3 initial geometry into a distorted cell

Figure 3.7 shows the formation of a Case 3 initial geometry as observed in actual Voronoi meshes. Consider a finite element mesh, in which cell *E* (not shown for clarity) meets its two neighbouring cells *C* and *D* through quadrilateral faces *CE* and *DE* (Figure 3.7a). In addition, cells *C*, *D*, and *E* are positioned between cells *A* and *B*, which remain separated by short edges *1*, *2* and *3*. This specific scenario may occur for sufficiently compressed cells experiencing the annealing process. To regain spherical geometries, cells *A* and *B* must expand in the vertical direction and contract in the horizontal direction. The same must also occur for cells *C*, *D*, and *E*. As a result, one may reasonably expect a final configuration where cell *A* and *B* touch while the horizontal contraction disjoins cell *E* from cells *C* and *D*.

25
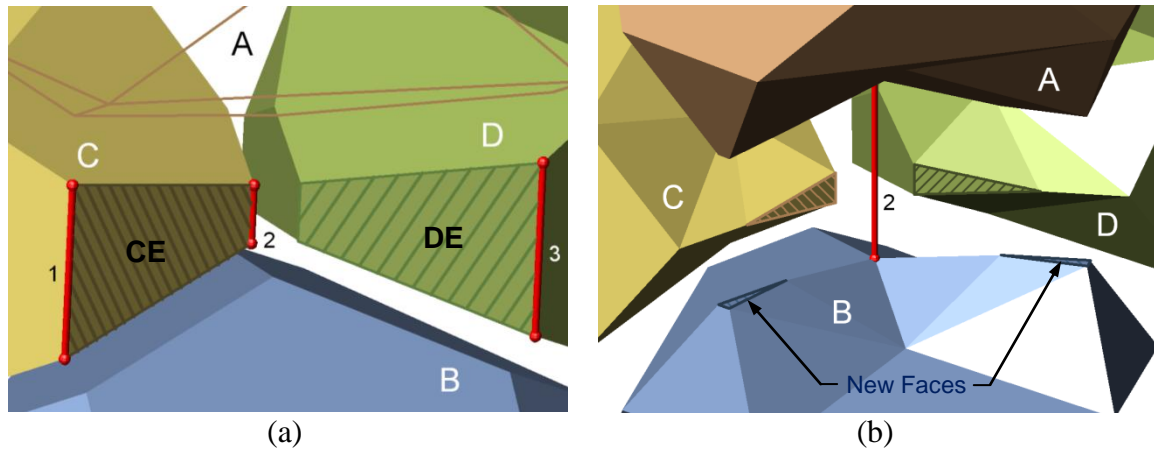
(a)   (b)

Figure 3.7: One possible formation of a Case 3 initial geometry

The presence of three short edges entails the execution of three Case 1 rearrangements. The order in which the three rearrangements are made is somewhat random due to the nature of numerical simulations. Yet, the problematic Case 3 initial geometry forms if edges *1* and *3* undergo neighbour changes before edge *2* does. Recall from before that quadrilaterals would reduce to triangles for the connected faces in Case 1 rearrangements. As shown in Figure 3.7b, edge *2* becomes part of two triangular faces. In addition, this neighbour change sequence produces an exception to the mesh geometric assumption; cells *A* and *B* are now connected through two newly created triangular faces (highlighted in blue in Figure 3.7b).

Distorted cells eventually lead to numerical crashes or ineffective volume constraints due to miscalculated cell volumes. Accordingly, a rearrangement algorithm is necessary for the Case 3 initial geometry, to more realistically replicate the interactions of real biological cells.

3.4.4 Case 3 Cell Rearrangement

With reference to Figure 3.8, the Case 3 cell rearrangement algorithm is designed to perform: 1) the separation of cell *E* from cells *C* and *D*, and 2) the joining of cells *A* and *B*. A summary of the rearrangement process is schematically presented in this figure.
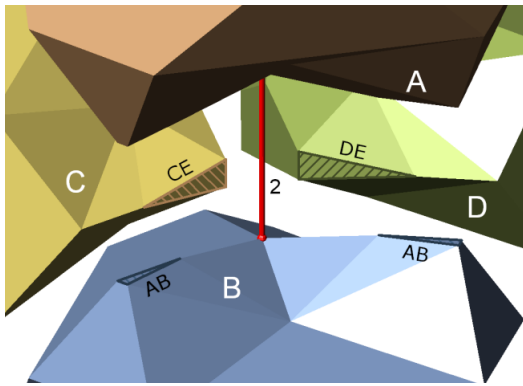
(a) 1 edge and 2 nodes are deleted.
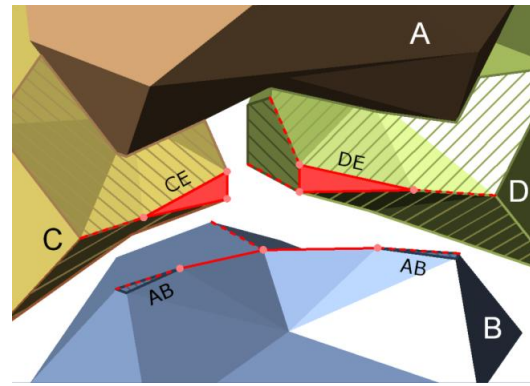
(b) 2 faces (red) are deleted. 5 faces (stripped) lose an edge.
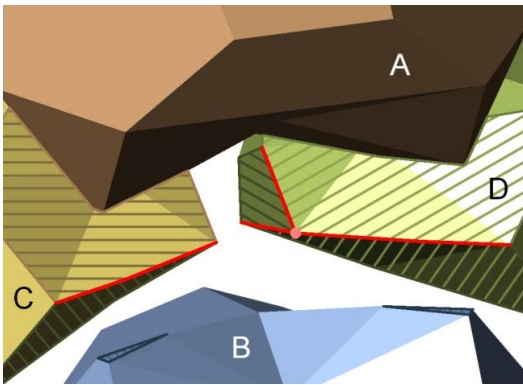
(c) 1 new node is created and 4 new edges are re-noded.
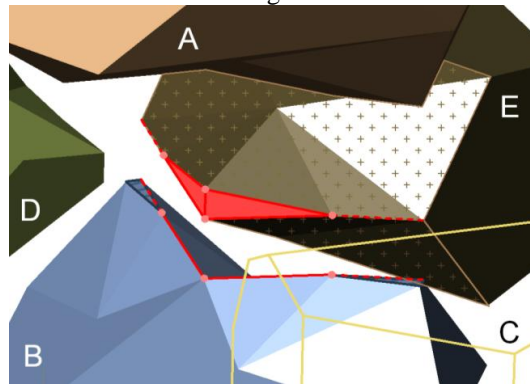
(d) 2 faces (red) are deleted. 2 faces lose two edges.
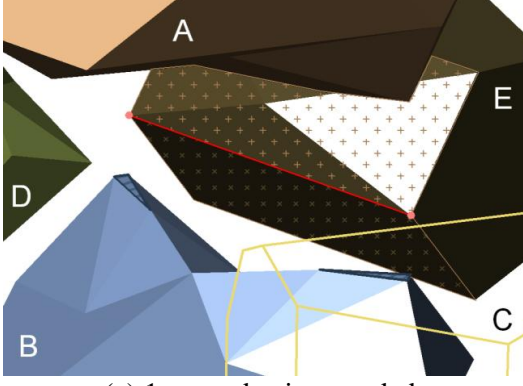
(e) 1 new edge is re-noded.
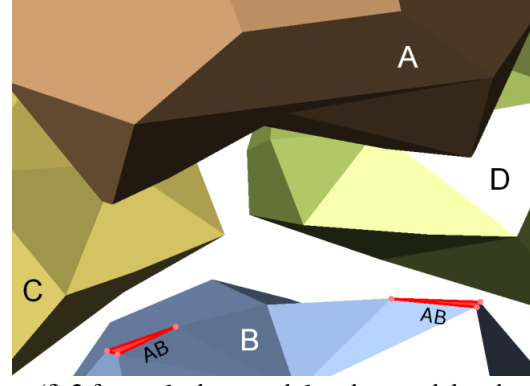
(f) 2 faces, 6 edges, and 6 nodes are deleted
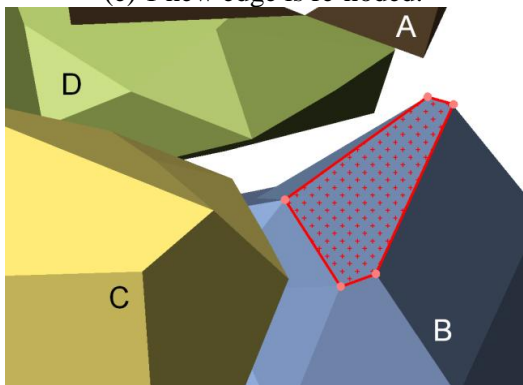
(g) 1 new face with 5 edges and 5 nodes are created
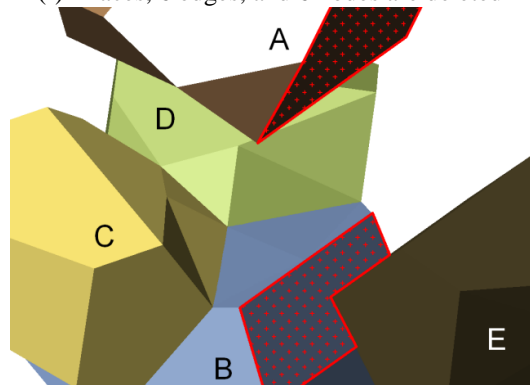
(h) Contact faces between cells *A, B* and *E* vary depending on the initial geometry

Figure 3.8: Case 3 cell rearrangement

As mentioned previously in Figure 3.7, cells *A* and *B* tend to expand vertically and move toward each other during the annealing process. This cell movement, in combination with specifically ordered Case 1 rearrangements, produces the Case 3 initial geometry in Figure 3.8a.

In Figure 3.8a the vertical short edge, which is part of two triangular faces (faces *CE* and *DE*), prompts the execution of a Case 3 cell rearrangement. First, the short edge is removed to allow an eventual full contact between cells *A* and *B*. Note that partial contact already exists between cells *A* and *B* via the two triangular faces (faces *AB*) resulted from earlier Case 1 rearrangements. Ultimately, the goal is to create a final configuration in which cells *A* and *B* meet at a single contact face. In addition, this contact face should be larger in area than the previous contact faces combined to reflect the attracting movement of cells *A* and *B*.

Figure 3.8b shows the deletion of faces *CE* and *DE*. This operation detaches both cells *C* and *D* from cell *E*, but creates undesirable openings on the surfaces of cells *C, D* and *E*. Therefore, geometric adjustments are necessary. As demonstrated in Figure 3.8c, the openings on cells *C* and *D* can be appropriately sealed by re-noding the four associated edges and removing an edge from each of the surrounding five faces. In Figure 3.8d a rotated view demonstrates the same deletion of faces *CE* and *DE* and the effect on cell *E*; a quadrilateral surface opening is produced. Figure 3.8e shows the sealing of this opening with the re-noding of an edge, in which the two surrounding faces consequently lose three edges each.

By this point, three issues remain: (1) creating additional contact area between cells *A* and *B* to account for the cell movement, (2) fixing the geometric inconsistency of multiple contact faces between two cells, and (3) accommodating the geometric adjustments made up to this point. The present algorithm adequately addresses these issues by replacing the two triangular faces *AB* in Figure 3.8f with a single pentagonal face (Figure 3.8g).

Figure 3.8h shows the final configuration of this Case 3 rearrangement, in which the newly created pentagonal face is appropriately the only interface between cells *A* and *B*.

28

In addition, cell **E** is detached from cells **C** and **D**. To summarize, Figure 3.9 illustrates the relevant faces before and after the Case 3 rearrangement. Note that the two-letter labels designate the two cells separated by each face.
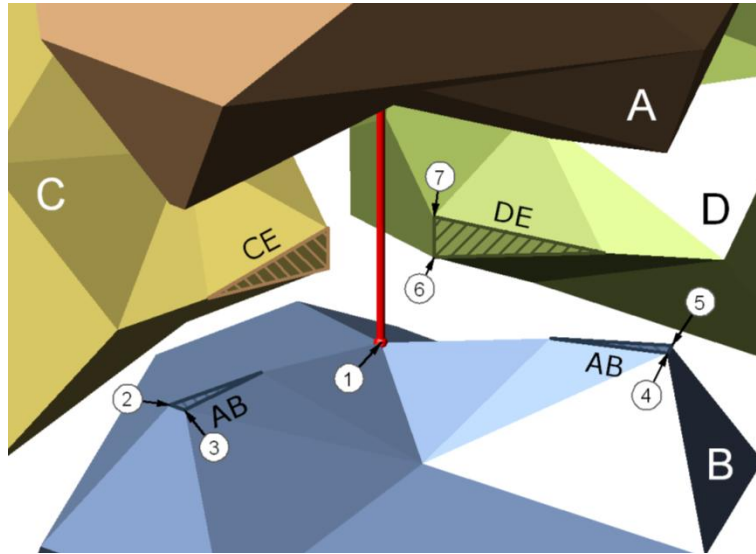
(a) Initial geometry
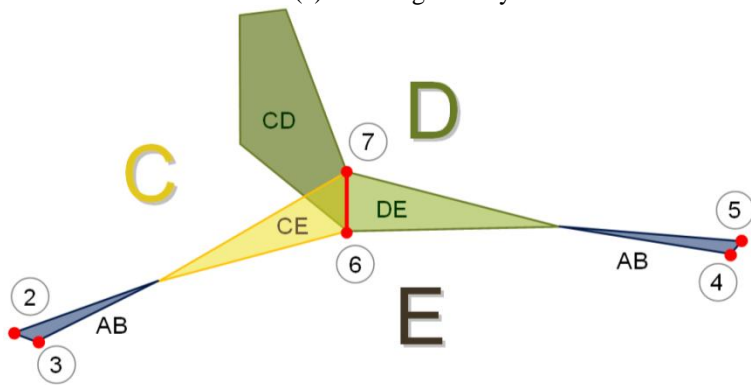
(b) Initial face and node detail
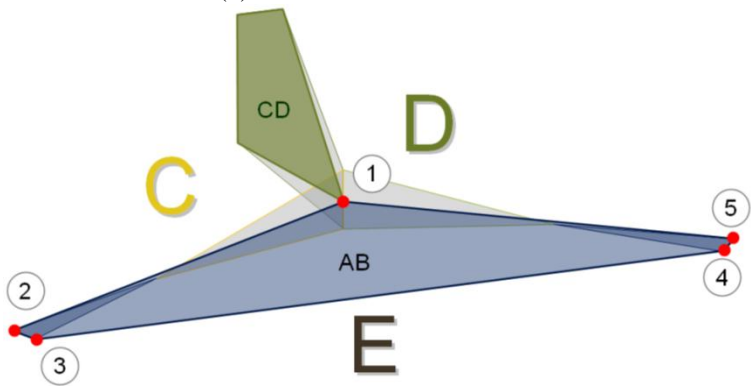
(c) Final face and node detail

Figure 3.9: Case 3 cell rearrangement – face and node details

3.4.5 Possible Case 4 Cell Rearrangement

The Case 4 initial geometry describes the situation where the short edge in question is part of three triangular faces. Though it has not been observed in actual FE meshes, one possible formation of a Case 4 initial geometry is proposed in Figure 3.10. In this proposed scenario, the cells are again sufficiently compressed in the vertical direction. As cells *A* and *B* regain spherical shapes by expanding vertically, cells *C*, *D*, and *E* (not shown in Figure 3.10) move away from the short edges to allow contact between cells *A* and *B*.
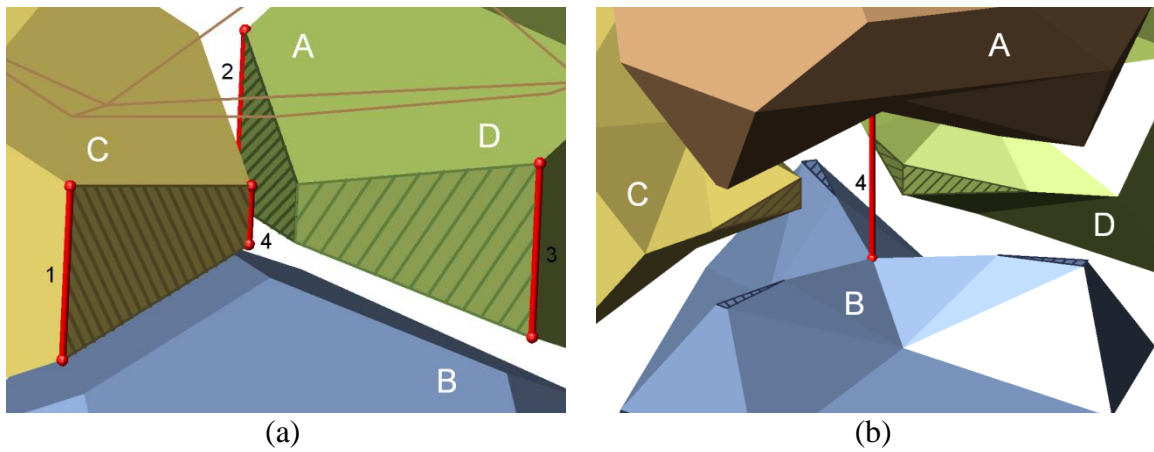
Figure 3.10: One possible formation of a Case 4 initial geometry

Cells *A* and *B* are initially separated by four edges and three quadrilateral faces. A Case 4 initial geometry (Figure 3.10b) forms if edges *1*, *2*, and *3* all undergo Case 1 rearrangements prior to edge *4*. The result is edge *4* as part of three triangular faces and cells *A* and *B* contacting at three small triangular faces. Figure 3.11 provides a solution for removing the remaining edge *4* and fixing the geometric inconsistency of multiple contact faces.

<div style="text-align:center">(a)   (b)</div>
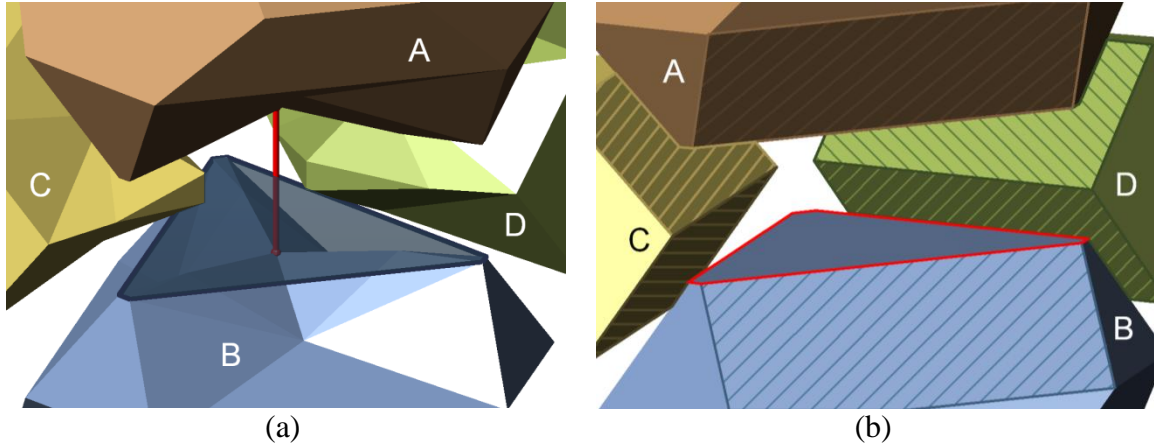
Figure 3.11: Proposed Case 4 cell rearrangement for implementation

In Figure 3.11a the short edge is replaced by a hexagonal face, which also integrates the three small triangular faces. Figure 3.11b shows that, to accommodate this operation, six surrounding faces are expected to require geometric adjustments. In the final configuration, cells A and B join via the newly created hexagonal face. No longer in contact with each other, cells C, D, and E are displaced away from the short edge.

3.5 Simulating Parallel Plate Compression

This section outlines the procedure for using the FE model to simulate a cell aggregate undergoing parallel plate compression, while suspended in the continuous phase of an immiscible fluid or the medium.

Emulsified cells are spherical in shape due to the cohesive forces at the cell-medium interface. Therefore, a Voronoi tessellation (Figure 3.12a) is allowed to round up under tension values in the ratio of $\gamma_{cc}{:}\gamma_{cm} = 1.0{:}1.5$, where γ_{cc} indicates the cell-cell interfacial tension and γ_{cm} denotes the cell-medium surface tension. This preliminary annealing process generates a near-spherical mesh (Figure 3.12b).
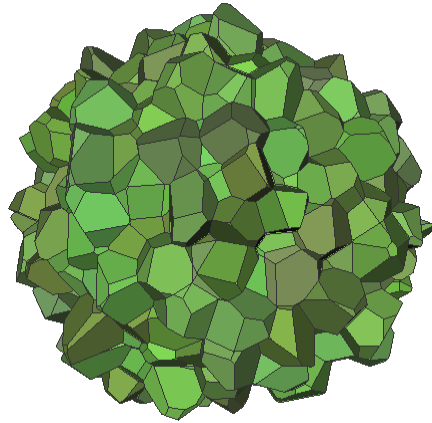
(a) Spherical Voronoi tessellation   (b) Annealed mesh
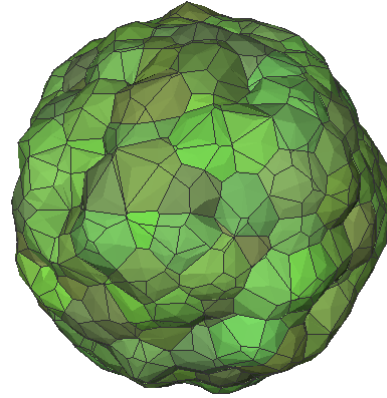
(c) Small faces are merged   (d) Further annealed mesh
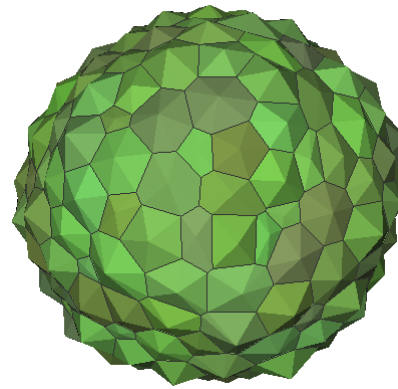
Figure 3.12: Near-spherical configurations

Subsequently, small faces on the mesh surface are merged (Figure 3.12c), so that each surface cell is exposed to the medium via only one face (Viens and Brodland 2007). As the medium is basically considered as a special cell type, this face-merging procedure is necessary in keeping consistency with our geometric restrictions (Section 3.1) and the cell rearrangement algorithm (Section 3.4).

In the final step, the mesh undergoes an additional annealing process to refine its spherical form. Figure 3.12d is the typical 454-cell starting configuration used in the parallel compression simulations in this study. The exterior faces appear circular and equal in terms of surface area. This outcome is desirable as the cells are monotypic; each cell strives to minimize its exposure to the medium with equal efforts. In addition, the convex nature of the surface faces is a result of the internal cell pressure.

32

The compression process is modeled by simultaneously moving the two polar nodes toward the mesh center along the compression or vertical axis at a constant rate (Figure 3.13).
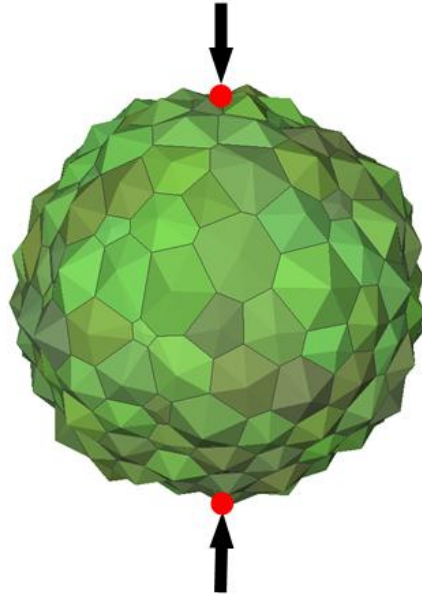
Figure 3.13: Moving the two polar nodes to simulate compression

In addition, appropriate boundary conditions are imposed to simulate the parallel plates. The present simulation considers frictionless and free lateral contact faces, i.e., the nodes touching the plates are fixed in the direction of compression, but are free to move across the plane. The finite element mesh undergoes significant deformation to become approximately halved in height (Figure 3.14).
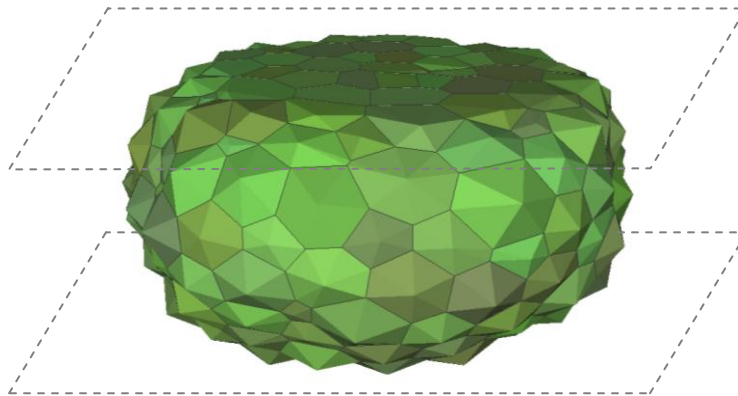
Figure 3.14: Compressed finite element mesh

The mesh is then allowed to anneal at that compression level until a state of equilibrium is reached. The anisotropy of individual cells, as later defined in Section 4.1, is monitored throughout the compression and annealing processes. To investigate whether locations within an aggregate influence the geometry of individual cells, each cell is categorized into one of three groups. Figure 3.15 demonstrates these three groups. Cells in contact with the compression plates are denoted by *plate*, whereas *medium* indicates cells exposed to the medium. The remaining surrounded cells are termed *interior*. In subsequent analyses, the cell properties reported are the averages for each group.
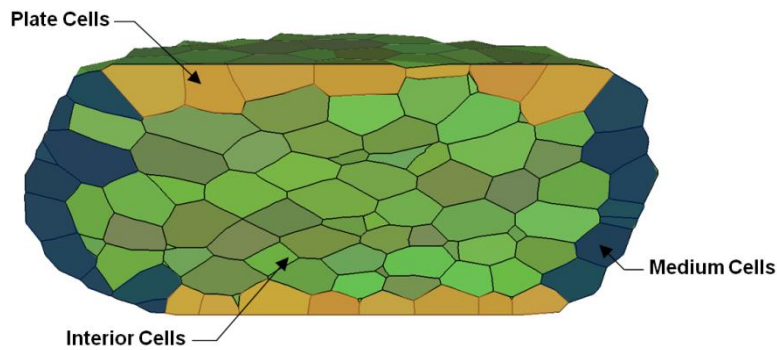
Figure 3.15: Cell location categorization by regions within the aggregate

To investigate the effects of different surface tensions, three FE models with different combinations of cell-cell interfacial tension γ_{cc}, cell-medium surface tension γ_{cm}, and cell-plate surface tension γ_{cp} (Table 3.1) are studied here. Also included is the viscosity μ value used in all simulation cases.

Table 3.1: Tension and viscosity values used for simulations

Case	γ_{cc}	γ_{cm}	γ_{cp}	μ
1	10000	10000	10000	
2	10000	15000	15000	2000
3	10000	15000	10000	

Case 1 describes the reference model with equal tension values: $\gamma_{cc} = \gamma_{cm} = \gamma_{cp}$. Case 2 is designed to reveal the effect of increasing the overall surface tension, which includes both γ_{cm} and γ_{cp}. Comparison between Case 1 and Case 3 shows the individual effect of γ_{cm}, while comparison between Case 2 and Case 3 demonstrates the result of varying γ_{cp}.

The value of γ_{cc} is kept constant for all cases, because previous simulations (Viens and Brodland 2007) have shown that changing γ_{cc} simply speeds up or slows down the annealing process. For example, doubling all γ_{cc} values in a model produces identical sequences of nodal displacement in half of the simulation time; doubling viscosity μ has the opposite effect. In other words, the ratio between γ_{cc} and μ affects the rate of interior cell shape change as later discussed in Section 5.1.2.

Lastly, a dimensionless approach is taken to allow comparison between different cell meshes. Parametric studies and theoretical considerations (Viens and Brodland 2007) show that this relationship can be non-dimensionalized by setting

$$\tau = \frac{3\gamma}{r\mu} t \qquad\qquad \text{Eq. 3.7}$$

where r is the radius of a spherical (isotropic) cell with the same volume, and t is the actual elapsed time in the simulation. Note that applying Eq. 3.7 normalizes the ratio between γ_{cc} and μ so that nodal movements between different cell meshes can be meaningfully contrasted.

4 Geometric Characterizations

Cells are convex polyhedra in the present FE model. Section 4.1 describes the "equivalent ellipsoid" method used to quantify the anisotropy of individual cells in the present study. In Section 4.2 the average anisotropy represented by a 2D cross section is defined, because we want to investigate the relationship between the geometric properties of 2D cross sections and 3D cell shapes.

4.1 Characterizing the Individual Cell Anisotropy

To characterize the shape of cells, we match each polyhedral cell with a solid and homogeneous ellipsoid that has the same inertia tensor. The geometric properties of this "equivalent ellipsoid" are then utilized to quantify cell anisotropy and orientation.

The concept of the inertia tensor and its inertial components are first introduced in Section 4.1.1. Section 4.1.2 subsequently provides a 2D example, in which inertial quantities are utilized to describe the anisotropy and orientation of a rigid body. Section 4.1.3 details the procedure of computing the inertia tensor of an arbitrary polyhedral. Lastly, the "equivalent ellipsoid" method is summarized in Section 4.1.4.

4.1.1 The Inertia Tensor

Typically used in applications of rotational dynamics, an inertia tensor I_{jk} is also capable of describing how the mass is distributed in rigid bodies.

$$I_{jk} = \begin{bmatrix} I_{xx} & I_{xy} & I_{xz} \\ I_{yx} & I_{yy} & I_{yz} \\ I_{zx} & I_{zy} & I_{zz} \end{bmatrix} \qquad \text{Eq. 4.1}$$

The diagonal quantities I_{xx}, I_{yy}, and I_{zz} are called the *moments of inertia* with reference to the x, y, and z axes, respectively, and are defined by Eq. 4.2 to Eq. 4.4.

$$I_{xx} = \int_m (y^2 + z^2)\, dm \qquad \text{Eq. 4.2}$$

$$I_{yy} = \int_m (x^2 + z^2)\, dm \qquad\qquad\qquad \text{Eq. 4.3}$$

$$I_{zz} = \int_m (x^2 + y^2)\, dm \qquad\qquad\qquad \text{Eq. 4.4}$$

where the variable of integration *m* is the mass and the integrand is the square of the perpendicular distance *r* to the corresponding rotating axis. Exemplified in Figure 4.1, these equations say that the moment of inertia for the larger point mass is $m_1 r_1{}^2$ and that of the smaller point mass is $m_2 r_2{}^2$ with respect to the axis of rotation.
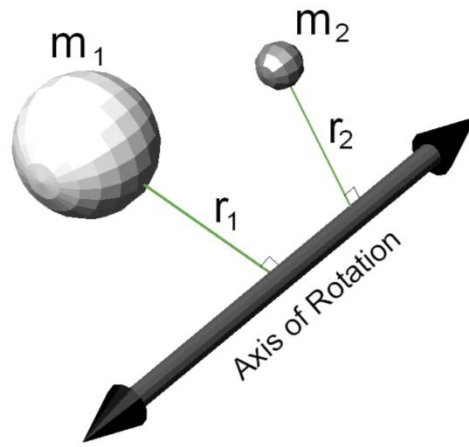
Figure 4.1: Two point masses around an axis of rotation

The non-diagonal quantities of I_{jk} are termed the *products of inertia*, as defined by Eq. 4.5 to Eq. 4.7.

$$I_{xy} = I_{yx} = -\int_m xy\, dm \qquad\qquad\qquad \text{Eq. 4.5}$$

$$I_{xz} = I_{zx} = -\int_m xz\, dm \qquad\qquad\qquad \text{Eq. 4.6}$$

$$I_{yz} = I_{zy} = -\int_m yz\, dm \qquad\qquad\qquad \text{Eq. 4.7}$$

Products of inertia are essentially a measure of symmetry. If an axis is perpendicular to the symmetric plane of the object, its associated products of inertia are zero. Consider a thin plate as shown in Figure 4.2.
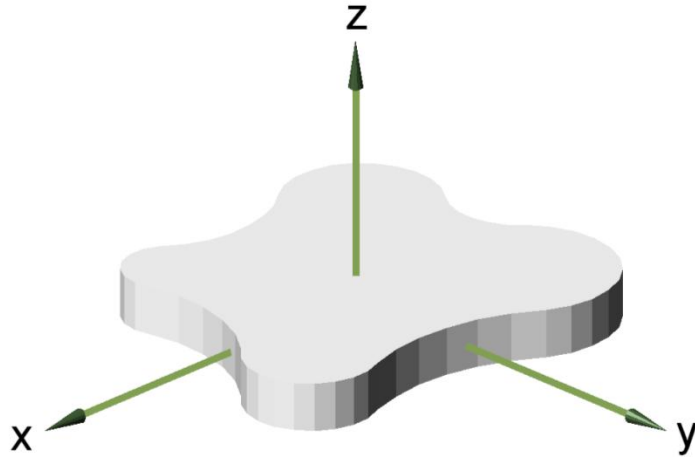
Figure 4.2: A thin plate that is symmetrical about the xy-plane

The plate centroid is located at the origin such that half of the plate is above the xy-plane and half is below. Hence, the xy-plane is a plane of symmetry and the products of inertia associated with the z axis ($I_{xz} = I_{zx} = I_{yz} = I_{zy}$) are all equal to zero.

4.1.2 Cell Anisotropy by Inertial Quantities – 2D Example

To illustrate how inertial quantities may be used to describe the anisotropy of a rigid body, we consider two equal-area ellipses with different x-radius a to y-radius b ratios of 3:1 and 3:4 (Figure 4.3).

(a)   (b)
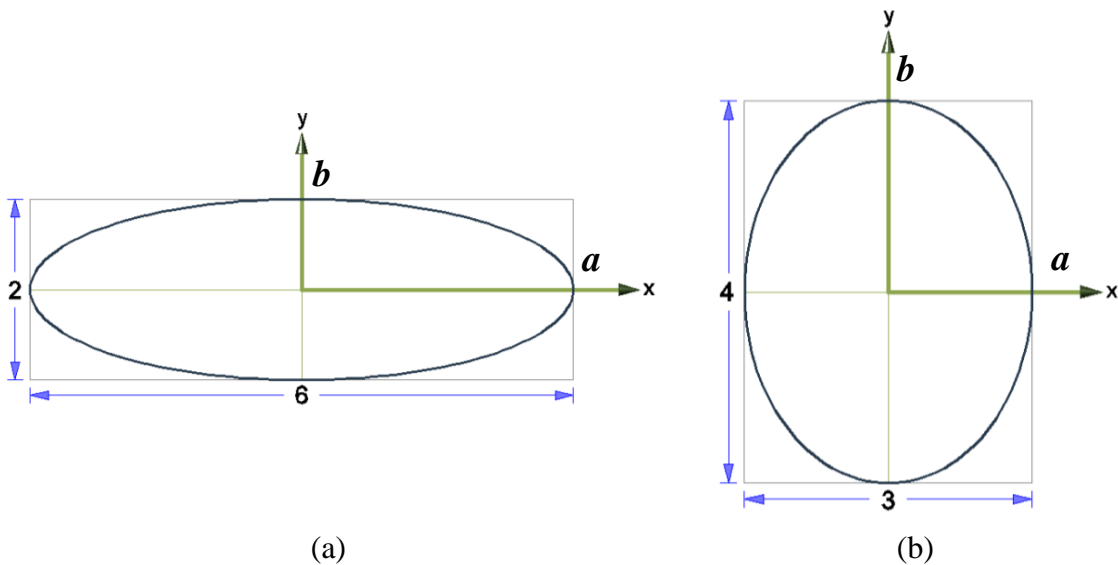
Figure 4.3: Ellipses with different aspect ratios

The moments of inertia about the x and y axes for ellipses are respectively defined as:

$$I_{xx} = \frac{1}{4}\pi a b^3 \qquad \text{Eq. 4.8}$$

$$I_{yy} = \frac{1}{4}\pi b a^3 \qquad \text{Eq. 4.9}$$

Table 4.1 lists the moment of inertia values for the two ellipses illustrated in Figure 4.3.

Table 4.1: Summary of moment of inertia values

Ellipse	(a)	(b)
I_{xx}	0.75 π	3 π
I_{yy}	6.75 π	1.6875 π
$\kappa\,(I_{xx}{:}\,I_{yy})^{0.5}$	1:3	4:3

Note that the elongation in a certain axis is appropriately reflected by a smaller moment of inertia value corresponding to that axis. In addition, an inspection of Eq. 4.8 and Eq. 4.9 reveals that the exact aspect ratio κ of an ellipse can be obtained by taking the square root of the ratio of the two moments of inertia. Section 4.2 utilizes this concept to characterize the 2D cross sections of cell meshes. Extending this concept to the 3D counterpart of ellipses, the aspect ratios for ellipsoids are similarly obtained in Section 4.1.4.

Inertial quantities can also be used to identify the orientation of an object. Figure 4.4 depicts an ellipse rotated to align with a new coordinate system $x'y'$.
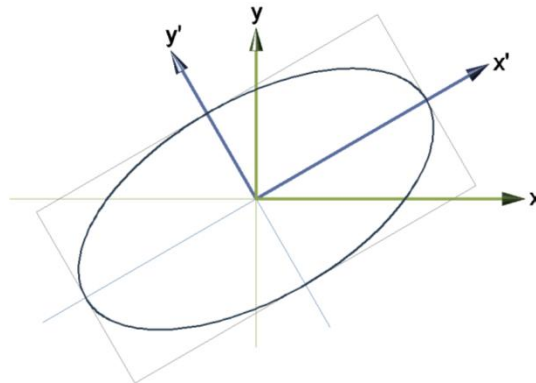
Figure 4.4: The orientation of an ellipse can be described by products of inertia

With Eq. 4.5 it can be shown that $I_{xy} \neq 0$ and $I_{yx} \neq 0$, while $I_{x'y'} = I_{y'x'} = 0$. The rotation required to achieve symmetries about a given coordinate system can define the orientation of an object. In other words, the *x'* and *y'* axes are aligned with the principal axes of the ellipse. Moreover, the inertia tensor of the ellipse in the rotated *x'y'* coordinate system only has values for its diagonal components, termed the principal moments of inertia. Thus, identifying the anisotropy and orientation of an object is manifest as an eigenvalue problem.

Section 4.1.4 extends the above concept of using inertial quantities to describe the anisotropy of 3D polyhedral cells. First, a method for calculating the inertia tensor of an arbitrary polyhedron is developed in the following section.

4.1.3 Polyhedral Inertia Tensor Calculation

Computing the inertia tensor of an arbitrary polyhedron can be done by partitioning it into several tetrahedra. The polyhedron is triangulated by rotating around its centroid such that the centroid is part of every tetrahedron (Figure 4.5).
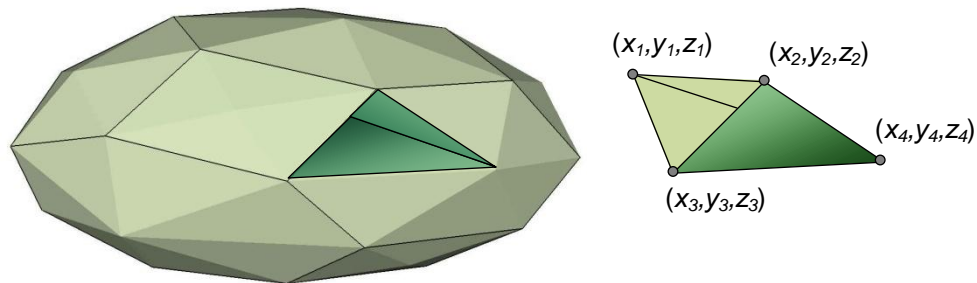
Figure 4.5: A triangulated polyhedron is consisted of many tetrahedra

If each tetrahedron inertia tensor is calculated with respect to the same reference system, the inertia tensor of the entire cell can be obtained as the sum of the tetrahedron inertia tensors.

The components in the tetrahedron inertia tensor I_{jk} (Eq. 4.1) can be individually obtained by integrating Eq. 4.2 to Eq. 4.7, or we can use the expressions formulated by Tonon (2004) to simplify this integration step. Tonon's formulation starts with an affine transformation, in which the tetrahedron is re-defined in a more convenient coordinate system for integration. Subsequently, the transformed integrand is solved alongside the

Jacobian determinant. The resulting integral is conveniently explicit in terms of the four vertex coordinates (x_i, y_i, z_i) $i = 1, \ldots, 4$ of a tetrahedron (Figure 4.5), as shown in the following equations:

$$
\begin{aligned}
I_{xx} = \rho \cdot V \cdot (y_1^2 + y_1 y_2 + y_2^2 + y_1 y_3 + y_2 y_3 \\
+ y_3^2 + y_1 y_4 + y_2 y_4 + y_3 y_4 + y_4^2 + z_1^2 + z_1 z_2 \\
+ z_2^2 + z_1 z_3 + z_2 z_3 + z_3^2 + z_1 z_4 + z_2 z_4 + z_3 z_4 + z_4^2)/10
\end{aligned}
\qquad \text{Eq. 4.10}
$$

$$
\begin{aligned}
I_{yy} = \rho \cdot V \cdot (x_1^2 + x_1 x_2 + x_2^2 + x_1 x_3 + x_2 x_3 \\
+ x_3^2 + x_1 x_4 + x_2 x_4 + x_3 x_4 + x_4^2 + z_1^2 + z_1 z_2 \\
+ z_2^2 + z_1 z_3 + z_2 z_3 + z_3^2 + z_1 z_4 + z_2 z_4 + z_3 z_4 + z_4^2)/10
\end{aligned}
\qquad \text{Eq. 4.11}
$$

$$
\begin{aligned}
I_{zz} = \rho \cdot V \cdot (x_1^2 + x_1 x_2 + x_2^2 + x_1 x_3 + x_2 x_3 \\
+ x_3^2 + x_1 x_4 + x_2 x_4 + x_3 x_4 + x_4^2 + y_1^2 + y_1 y_2 \\
+ y_2^2 + y_1 y_3 + y_2 y_3 + y_3^2 + y_1 y_4 + y_2 y_4 + y_3 y_4 + y_4^2)/10
\end{aligned}
\qquad \text{Eq. 4.12}
$$

$$
\begin{aligned}
I_{yz} = I_{zy} = -\rho \cdot V \cdot (2 y_1 z_1 + y_2 z_1 + y_3 z_1 + y_4 z_1 \\
+ y_1 z_2 + 2 y_2 z_2 + y_3 z_2 + y_4 z_2 + y_1 z_3 + y_2 z_3 + 2 y_3 z_3 \\
+ y_4 z_3 + y_1 z_4 + y_2 z_4 + y_3 z_4 + 2 y_4 z_4)/20
\end{aligned}
\qquad \text{Eq. 4.13}
$$

$$
\begin{aligned}
I_{xz} = I_{zx} = -\rho \cdot V \cdot (2 x_1 z_1 + x_2 z_1 + x_3 z_1 + x_4 z_1 \\
+ x_1 z_2 + 2 x_2 z_2 + x_3 z_2 + x_4 z_2 + x_1 z_3 + x_2 z_3 + 2 x_3 z_3 \\
+ x_4 z_3 + x_1 z_4 + x_2 z_4 + x_3 z_4 + 2 x_4 z_4)/20
\end{aligned}
\qquad \text{Eq. 4.14}
$$

$$
\begin{aligned}
I_{xy} = I_{yx} = -\rho \cdot V \cdot (2 x_1 y_1 + x_2 y_1 + x_3 y_1 + x_4 y_1 \\
+ x_1 y_2 + 2 x_2 y_2 + x_3 y_2 + x_4 y_2 + x_1 y_3 + x_2 y_3 + 2 x_3 y_3 \\
+ x_4 y_3 + x_1 y_4 + x_2 y_4 + x_3 y_4 + 2 x_4 y_4)/20
\end{aligned}
\qquad \text{Eq. 4.15}
$$

Eq. 4.10 to Eq. 4.15 express the inertial components with respect to the origin as simple quadratic polynomials of the vertex coordinates, multiplied by the volume V and the density ρ of the tetrahedron. Having obtained the tetrahedron inertia tensor I_{jk}, the inertia tensor of the entire polyhedral cell is calculated as the sum of all the individual I_{jk}:

$$
I_{cell} = \sum_i (I_{jk})_i
\qquad \text{Eq. 4.16}
$$

However, to find the principal moments and principal axes of the polyhedral cell, the inertia tensor I'_{cell} relative to the cell centroid should be calculated according to the parallel axis theorem:

$$
I'_{cell} = I_{cell} - Mass \cdot
\begin{bmatrix}
Y^2 + Z^2 & -XY & -XZ \\
-XY & X^2 + Z^2 & -YZ \\
-XZ & -YZ & X^2 + Y^2
\end{bmatrix}
\qquad \text{Eq. 4.17}
$$

where X, Y, Z are the Cartesian coordinates of the cell centroid.

4.1.4 Cell Anisotropy by the Equivalent Ellipsoid Method

The inertia tensor of an arbitrary polyhedron has been calculated in the previous section. In the "equivalent ellipsoid" method where cells are represented by solid and homogeneous ellipsoids, we require an ellipsoid (Figure 4.6b), as defined by its three radii a, b, and c, that has the same inertia tensor as the polyhedral cell (Figure 4.6a).
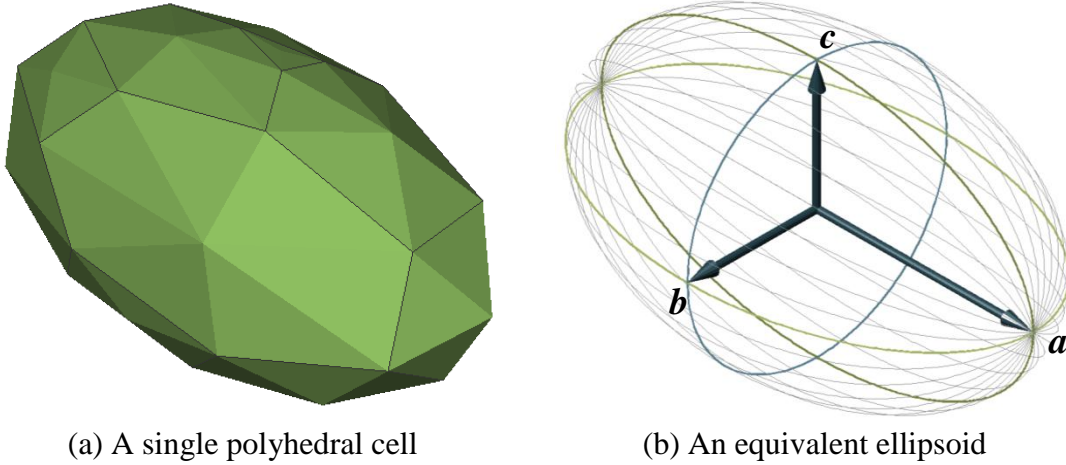
(a) A single polyhedral cell   (b) An equivalent ellipsoid
Figure 4.6: 3D description of cell orientation and anisotropy

Analogous to the ellipse example in Section 4.1.2, the principal axes of the polyhedral cell are found by rotating the inertia tensor I'_{cell} into a specific coordinate system where I'_{cell} becomes a diagonal matrix. This procedure emerges as a classic eigenvector problem. Each eigenvector e_i of I'_{cell} represents a principal axis of the cell, while the eigenvalues λ_i are the principal moments of inertia. This study defines the orientation of the cell to be the direction corresponding to the largest λ_i. The inertia tensor I'_{cell} is real and symmetric; therefore, its eigenvalues are guaranteed to be real and its eigenvectors to be orthogonal.

Imagine an ellipsoid whose semi-axes are aligned with the directions specified by the eigenvectors of I'_{cell} (Figure 4.6b). The lengths of the three principal radii $a \geq b \geq c$ can be calculated based on the eigenvalues of I'_{cell}. We know that the principal moments of inertia (I_A, I_B, I_C) of an ellipsoid of mass M with principal radii a, b, c are given by:

$$I_A = \frac{M(b^2 + c^2)}{5}$$

Eq. 4.18

42

$$I_B = \frac{M(a^2 + c^2)}{5} \qquad \text{Eq. 4.19}$$

$$I_C = \frac{M(a^2 + b^2)}{5} \qquad \text{Eq. 4.20}$$

To generate an ellipsoid with an inertia tensor equal to that of the polyhedral cell, we equate I_A, I_B, and I_C respectively to the three eigenvalues of I'_{cell}:

$$I_A = \lambda_1 \qquad \text{Eq. 4.21}$$

$$I_B = \lambda_2 \qquad \text{Eq. 4.22}$$

$$I_C = \lambda_3 \qquad \text{Eq. 4.23}$$

Inverting the above system of equations and solving for a, b, c produce the following equations:

$$a = \sqrt{\frac{5(\lambda_2 + \lambda_3 - \lambda_1)}{2M}} \qquad \text{Eq. 4.24}$$

$$b = \sqrt{\frac{5(\lambda_1 + \lambda_3 - \lambda_2)}{2M}} \qquad \text{Eq. 4.25}$$

$$c = \sqrt{\frac{5(\lambda_1 + \lambda_2 - \lambda_3)}{2M}} \qquad \text{Eq. 4.26}$$

With $a \geq b \geq c$, the anisotropy of an ellipsoid can be defined by the following aspect ratios:

$$\kappa_1 = \frac{a}{c} \qquad \text{Eq. 4.27}$$

$$\kappa_2 = \frac{b}{c} \qquad \text{Eq. 4.28}$$

For instance, a sphere has both aspect ratios valued at 1, while the aspect ratios of a compressed cell exhibit the following relationship: $\kappa_1 \geq \kappa_2 \geq 1$. In subsequent analyses only κ_1 is referred to as it represents the ratio between the maximum and minimum principal radii. The "equivalent ellipsoid" method is a well-behaved way for identifying

the orientation and anisotropy of individual cells, especially with respect to coordinate transformations.

4.2   Characterizing the Mesh Cross Sections

The method for characterizing the anisotropy of 3D cells has been established in the previous section. However, physical measurements of this geometric property are often restricted by the delicate nature of real cell specimens, and non-invasive methods are necessary. Therefore, if we can establish a correlation between the extracted 2D image data and the actual 3D geometry of cells, a significant efficiency in data interpretation can be achieved. Accordingly, this study intends to explore this possibility by examining the finite element meshes and their 2D cross sections. First, we define a method for characterizing the average anisotropy of a given cross section.

Consider a polyhedral cell and its cross section at an arbitrary plane as shown in Figure 4.7.

(a)   (b)
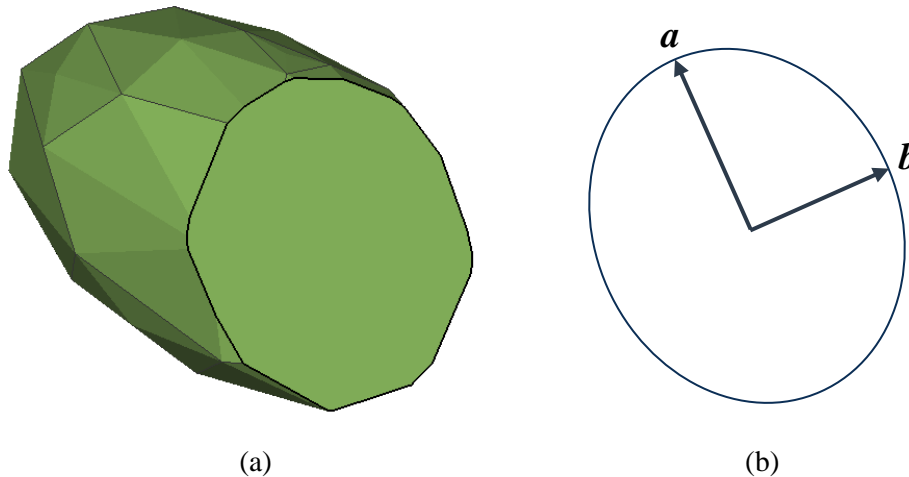
Figure 4.7: A single polyhedral cell with its cross section at an arbitrary plane

This study defines the anisotropy of 3D cells with the "equivalent ellipsoid" method. In a similar fashion, the aspect ratio of the 2D cross section can be quantified by finding an equivalent ellipse. The question is whether an elongated ellipsoid has cross sections showing equally or similarly elongated ellipses. Accordingly, we perform statistical

analyses to determine how representative equivalent ellipses are of their equivalent ellipsoids, in terms of average cell anisotropy, in a given cross section.

Two different sets of planar cross sections are obtained for analysis, as schematically illustrated in Figure 4.8.
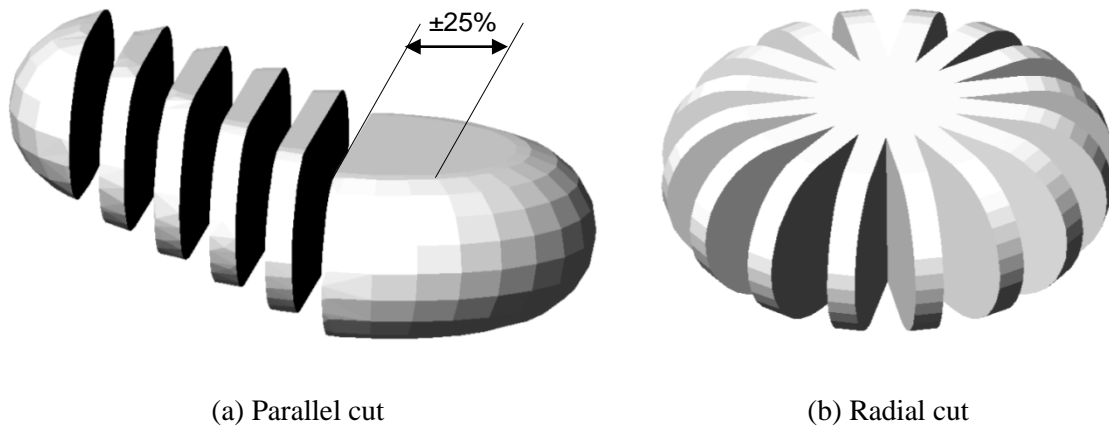
(a) Parallel cut   (b) Radial cut
Figure 4.8: Two types of planar cross sections

In Figure 4.8 each slice represents a cutting plane. For each mesh, 36 parallel cross sections (Figure 4.8a) and 36 radial cross sections (Figure 4.8b) are generated for statistical analyses. Note that the parallel planes are selected to evenly cut the aggregate bounded by ±25% offset from the mesh center, so that a sufficient sample of cells is obtained. The radial sections evenly segment the mesh at 5° increments. Figure 4.9 illustrates a sample cross section.
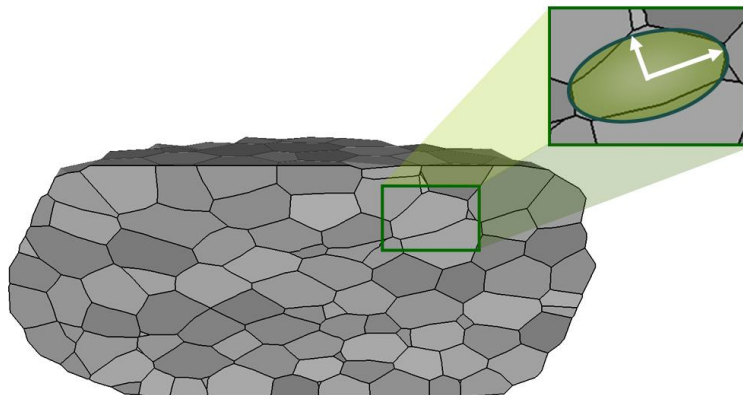
Figure 4.9: A typical cross section

The aspect ratio κ of each 2D cell cross section is calculated using the method in Section 4.1.2, hereby termed the "equivalent ellipse" method. As discussed, the κ of an ellipse is determined by taking the square root of the ratio of the two principal moments of inertia. Subsequently, the values of the aspect ratio are averaged for each cell location group, as defined previously in Figure 3.15.

5 Results

This chapter presents the results from parallel plate compression simulations of a 3D cell aggregate. In Section 5.1 we examine how cell shape history is affected by the surface and interfacial tensions. A theoretical relationship between cell shape history and interfacial tensions is formulated and verified with numerical results, to enable the estimation of cell-cell interfacial tensions for other laboratory experiments or numerical simulations. To provide increased efficiency in data extraction, Section 5.2 explores the potential of correlating 2D geometric properties of a cross section to 3D cells in a mesh. The simulation results are also compared to a scanning electron micrograph of a fractured aggregate.

For analyses, this study defines the degree of compression ξ as the following dimensionless displacement:

$$\xi \equiv \frac{R - h}{R} \qquad \text{Eq. 5.1}$$

where R is the initial aggregate radius, and h is the vertical distance from the parallel plates to the center of the cell mesh (Figure 5.1).
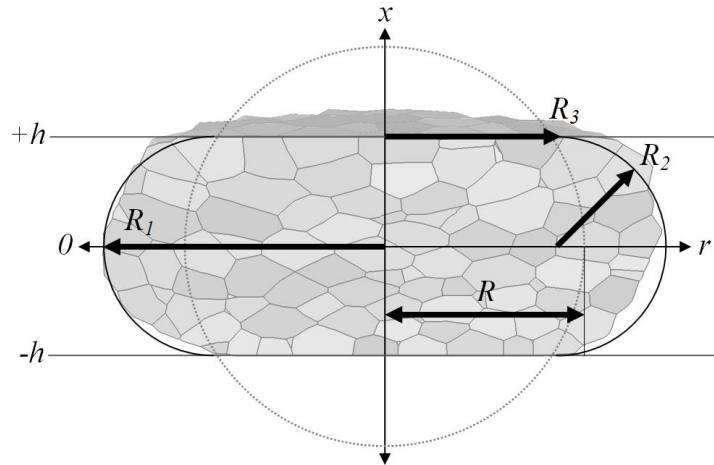
Figure 5.1: An aggregate of initial radius R compressed by parallel plates located at $x = \pm h$

Figure 5.1 also identifies three radii (R_1, R_2, and R_3) referred by analyses in the later sections.

5.1 Cell Anisotropy versus Annealing Time

As mentioned previously, initially flattened cells are able to slip past one another and return to a nearly isotropic configuration, during prolonged compression. This phenomenon can be seen in the cross sections (Figure 5.2) through the center of the aggregate at two different simulation times. Cross sections in the left column are taken immediately after compression from meshes of the three simulation cases (see Table 3.1), while the right column contains the annealed cases.
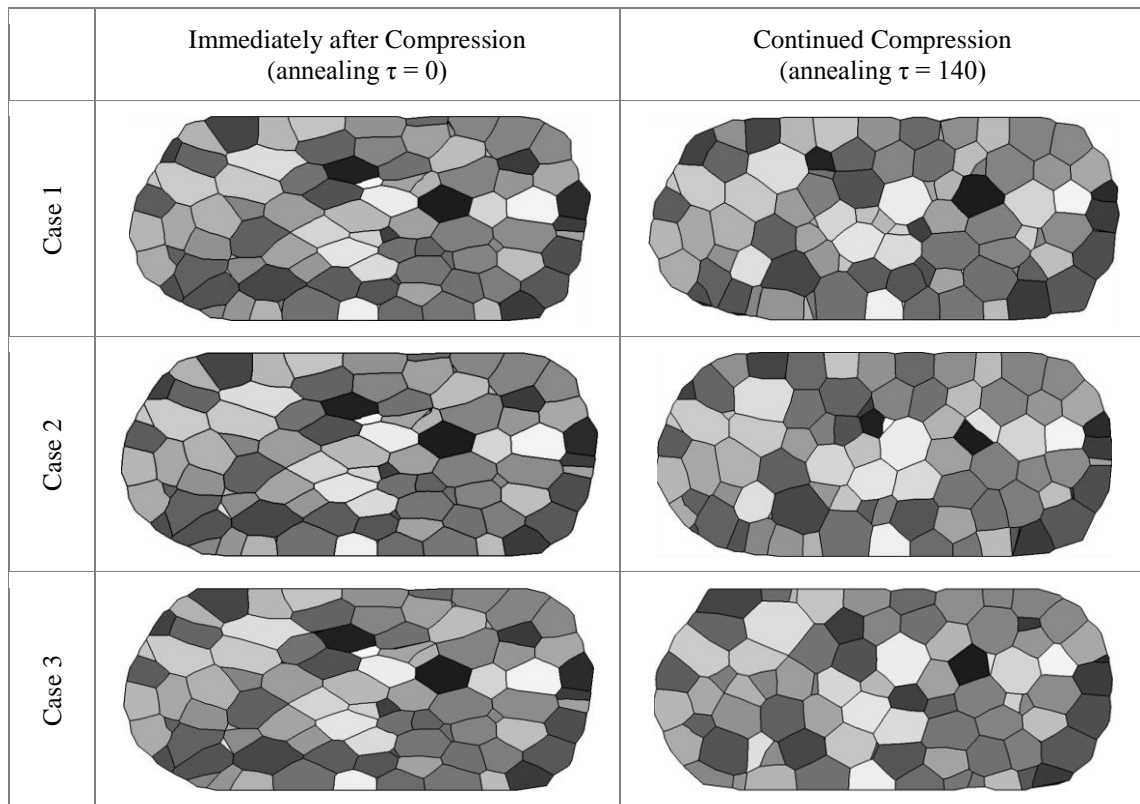
Figure 5.2: Cross sections of the cell aggregate

Each set of cross sections demonstrates the rounding and relative movements of cells, which are produced by the annealing process. Also note that the aggregate side profiles for Case 2 and Case 3 are slightly more circular due to the increased γ_{cm}.

The next section examines the effects of γ_{cm} and γ_{cp} on cell shape history in different regions of the aggregate. To start, the present study comments on the value of average κ_1 of an annealed mesh. For Figure 5.3 to Figure 5.5, the configurations existing at $\tau = 0$ and $\tau = 140$ should theoretically have their average κ_1 for **Interior** cells equal (or close) to 1. However, as will be seen, this value for reputedly isotropic cells in aggregate ranges from 1.3 to 1.5. Similarly in 2D, the average κ for Voronoi planar aggregates after annealing is found to be approximately 1.25.

This departure from 1 can be caused by the reduced flexibility of polyhedral cell faces to become curved within an aggregate. In addition, the surrounding cells inflict extra constraints on how a cell may re-align itself. Ketcham (2005) also observed slight anisotropies in interior rock crystals using high-resolution X-ray computed tomography (HRXCT). The distribution of garnet aspect ratios has a consistent mean value of about 1.4 to 1.5 that persists among all size classes. Hence, though not mathematically isotropic, the aggregated cells at $\tau = 0$ and $\tau = 140$ are considered to be annealed and at a state of equilibrium in this study.

5.1.1 The Effect of Surface Tension

To reveal the effect of overall surface tension, namely both γ_{cm} and γ_{cp}, Figure 5.3 plots the average κ_1 versus τ for Case 1 and Case 2.
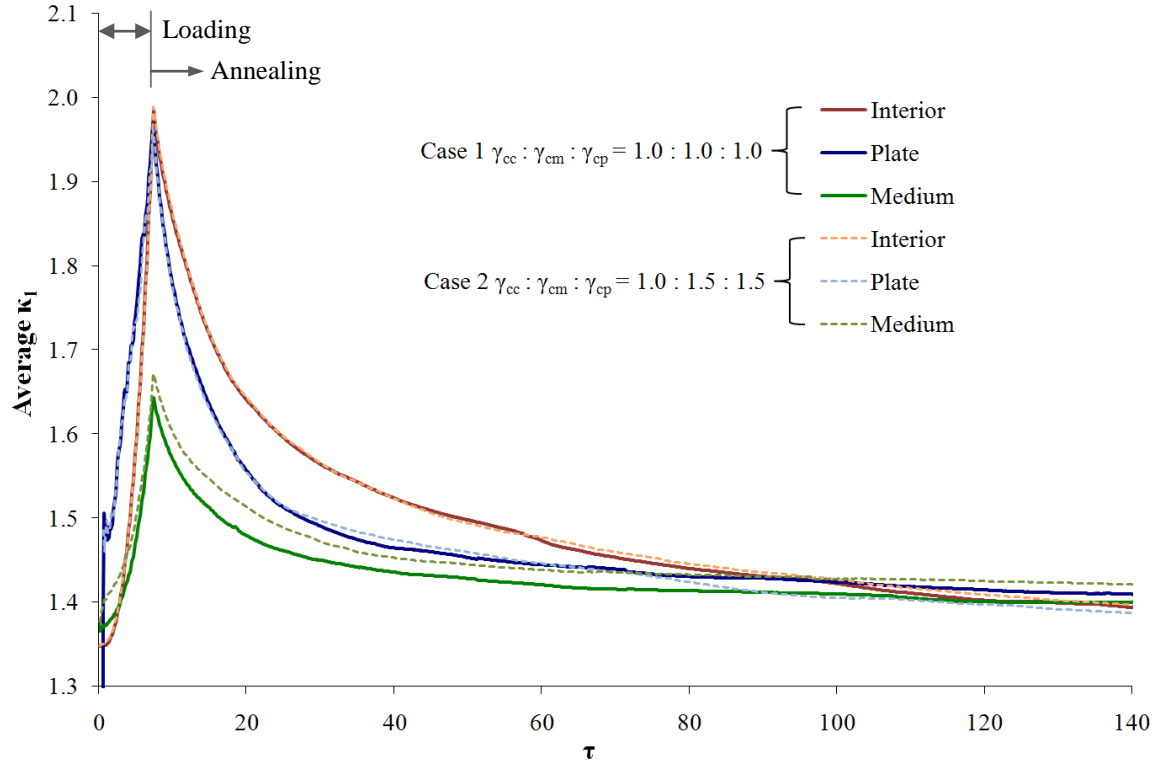
Figure 5.3: Effect of overall surface tension on the history of average κ_I

The interior cells remain more compressed during the initial annealing process, and are essentially unaffected by changes in the surface tension. Compared to the interior group, cells exposed to the medium anneal at a slower rate, as their surfaces are confined to the surface of the mass. The dashed green line of Case 2 shows that increasing the surface tension further reduces the rate of cell rounding. The most rapid annealing is observed for cells in contact with the compression plates (blue lines in Figure 5.3). This result may be attributed to the boundary condition that allows nodes on the plates to move freely within the horizontal plane.

To show the individual effects of medium and plate surface tensions, Figure 5.4 plots the average κ_I versus τ for Case 1 and Case 3, and Figure 5.5 shows the comparison between Case 2 and Case 3.
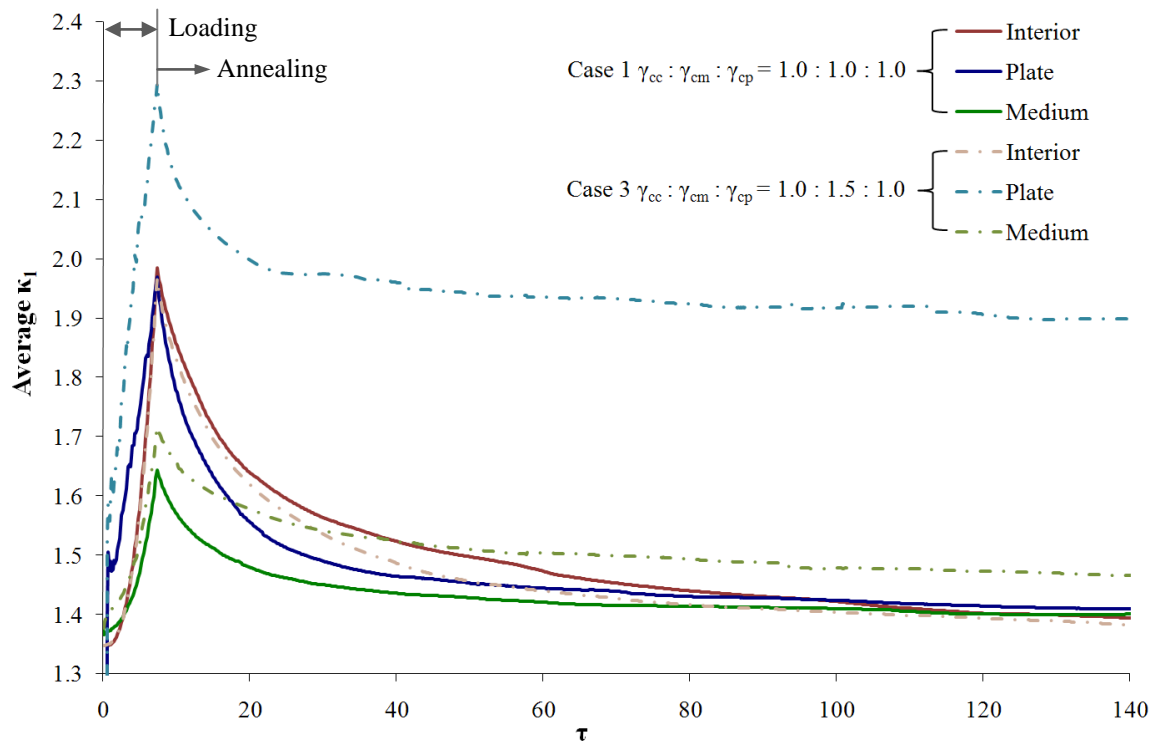
Figure 5.4: Effect of medium surface tension on the history of average κ_1
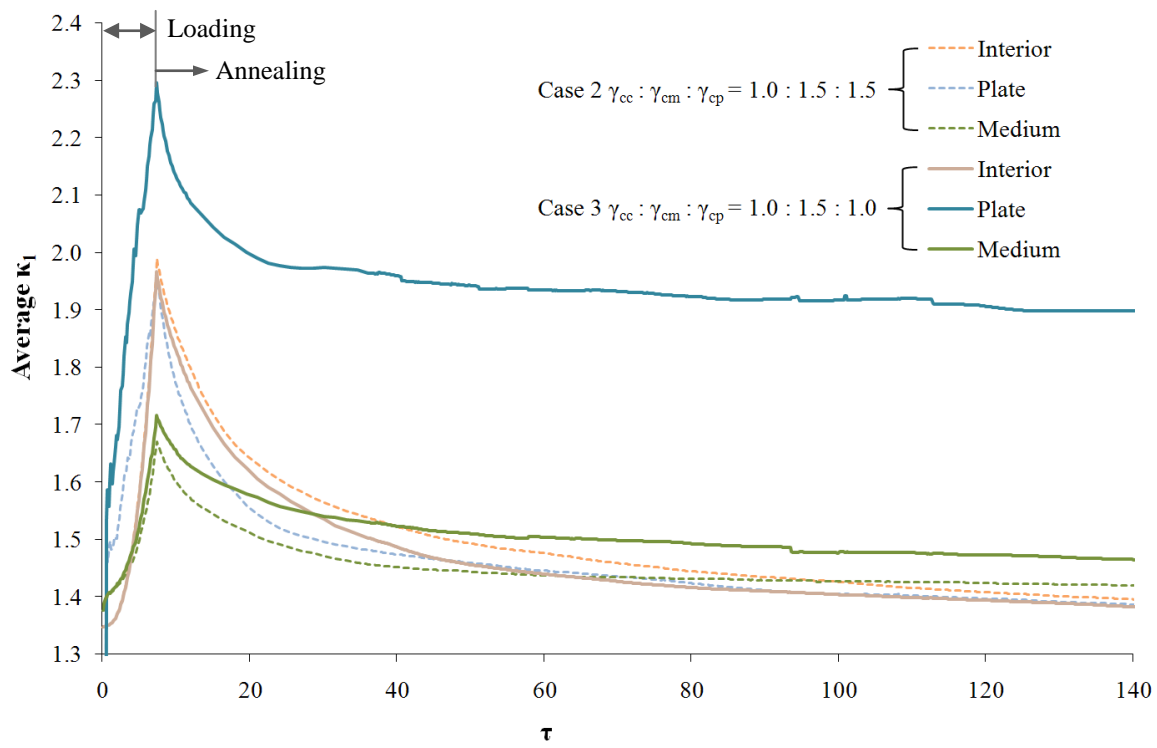
Figure 5.5: Effect of plate surface tension on the history of average κ_1

Similar phenomena, as previously described for Figure 5.3, are also evident in Figure 5.4 and Figure 5.5 in terms of the annealing rate and the anisotropy for different cell groups. The exception is for the plate cells in the absence of equally increased γ_{cp}. These cells equilibrate to highly compressed geometries ($\kappa_1 \approx 1.9$). The stronger γ_{cm} prevents the plate cells from moving out of the cylindrical region defined by R_3. As a result, they are in some way interior cells cut horizontally in half by the compression plates. This analogy explains their annealed κ_1 of approximately 2. The curve for the interior cells of Case 3 decays at a faster rate, but eventually reaches an equilibrium level similar to the ones for Case 1 and Case 2.

To summarize, the shapes of plate and medium cells are influenced by the additional geometric constraints imposed by the surface tensions and boundary conditions, whereas the interior cells are largely unaffected by those factors. As will be seen in Section 5.1.2, geometries of the interior cells are mainly governed by γ_{cc} and μ.

5.1.2   The Effects of Interfacial Tension and Viscosity

Here we develop a formula that can be used to calculate the contribution of γ_{cc} and μ to the rate of cell shape change. As mentioned, the behaviours of biological cells in aggregates are influenced by their interfacial tension γ_{cc} and effective cytoplasm viscosity μ (Forgacs 1998). Considering these two factors, this section analyzes the mechanics of a single, isolated cell undergoing the annealing process using the principles of conservation of energy.

Figure 5.6 shows an ellipsoidal cell compressed along the x-axis. An ellipsoidal geometry is considered because of its intuitive behaviour and because it provides a prototype for the analysis of cell aggregates. Assuming isotropic material properties, the deformed cell under uniaxial compression can be represented by an oblate spheroid having principal radii $a = b > c$.
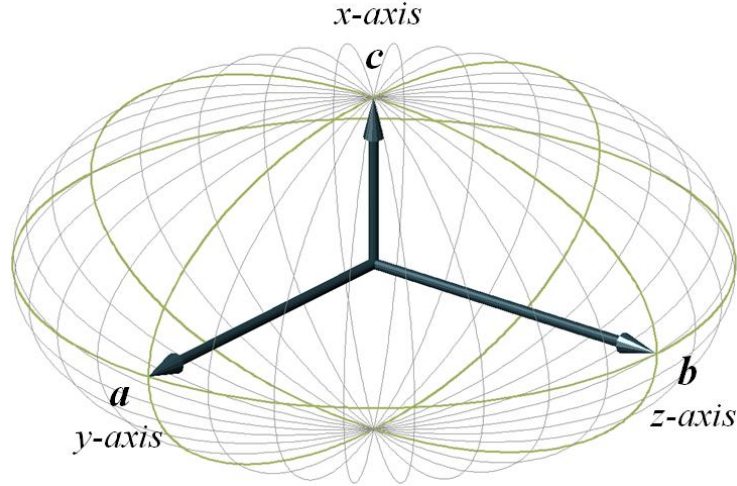
Figure 5.6: Ellipsoidal cell model

With reference to Figure 5.6, the volume V and the cell aspect ratio κ of an oblate spheroid can be defined as:

$$V = \frac{4}{3}\pi a^2 c \qquad \text{Eq. 5.2}$$

$$\kappa = \frac{a}{c} \qquad \text{Eq. 5.3}$$

Rearranging the equations allows the cell dimensions to be calculated for specified values of V and κ:

$$a = \sqrt[3]{\frac{3V\kappa}{4\pi}} \qquad \text{Eq. 5.4}$$

$$c = \sqrt[3]{\frac{3V}{4\pi\kappa^2}} \qquad \text{Eq. 5.5}$$

The rate $\dot{W}_\gamma$ at which work is done to the ellipsoidal cell by an interfacial (surface) tension γ_{cc} assumed to act on the cell surface A, when κ changes at rate $d\kappa/dt$, is defined as:

$$\dot{W}_\gamma = \gamma_{cc}\frac{dA}{d\kappa}\frac{d\kappa}{dt} \qquad \text{Eq. 5.6}$$

The surface area A of an oblate spheroid can be expressed as a function of κ by utilizing Eq. 5.4 and Eq. 5.5 (Selby 1965):

$$
\begin{aligned}
A &= 2\pi \left[a^2 + c^2 \frac{\tanh^{-1}\left(\sin\left(\cos^{-1}\left(\frac{c}{a}\right)\right)\right)}{\sin\left(\cos^{-1}\left(\frac{c}{a}\right)\right)} \right] \\
&= 2\pi \left[\left(\frac{3V\kappa}{4\pi}\right)^{\frac{2}{3}} + \left(\frac{3V}{4\pi\kappa^2}\right)^{\frac{2}{3}} \left(\frac{\tanh^{-1}\left(\sin\left(\cos^{-1}\left(\frac{1}{\kappa}\right)\right)\right)}{\sin\left(\cos^{-1}\left(\frac{1}{\kappa}\right)\right)} \right) \right]
\end{aligned}
\qquad \text{Eq. 5.7}
$$

Under the assumptions of a uniform strain state within the cell and a constant cell volume during annealing, the rate $\dot{U}_\mu$ at which strain energy is being stored in the deformed cell can be written as:

$$
\begin{aligned}
\dot{U}_\mu &= \frac{V}{2}\left(\sigma_x \dot{\varepsilon}_x + \sigma_y \dot{\varepsilon}_y + \sigma_z \dot{\varepsilon}_z + \tau_{xy}\dot{\gamma}_{xy} + \tau_{xz}\dot{\gamma}_{xz} + \tau_{yz}\dot{\gamma}_{yz}\right) \\
&= \frac{V}{2}\left(\sigma_x \dot{\varepsilon}_x + 2\sigma_y \dot{\varepsilon}_y\right)
\end{aligned}
\qquad \text{Eq. 5.8}
$$

where σ_i is the normal stress and $\dot{\varepsilon}_i$ is the normal strain rate in the i direction, τ_{ij} is the shear stress and $\dot{\gamma}_{ij}$ is the shear strain rate in the ij plane. Material isotropy provides the simplification of $\sigma_y \dot{\varepsilon}_y = \sigma_z \dot{\varepsilon}_z$, and geometric orthogonality allows the shear components to be set to zero.

The normal stress σ_i can be related to the normal strain rate $\dot{\varepsilon}_i$ through μ. First, consider the parallel between shear strain γ in a material described by shear modulus G and shear strain rate $\dot{\gamma}$ in a material described by viscosity μ. Stress and strain transformation concepts can be used to demonstrate the existence of a state of pure shear where $\dot{\gamma} = -\dot{\varepsilon}_x = \dot{\varepsilon}_y$. Furthermore, one can equate elastic modulus E to $3G$ for an incompressible fluid (Poisson ratio $\upsilon = 0.5$) with the following relationship:

$$
E = 2G(1 + \upsilon)
\qquad \text{Eq. 5.9}
$$

Hence, the incremental generalized Hooke's law for an incompressible fluid with an effective viscosity μ can be written as:

$$\dot{\varepsilon}_x = \frac{1}{3\mu}\left[\sigma_x - \frac{1}{2}(\sigma_y + \sigma_z)\right] \qquad \text{Eq. 5.10}$$

$$\dot{\varepsilon}_y = \frac{1}{3\mu}\left[\sigma_y - \frac{1}{2}(\sigma_x + \sigma_z)\right] \qquad \text{Eq. 5.11}$$

$$\dot{\varepsilon}_z = \frac{1}{3\mu}\left[\sigma_z - \frac{1}{2}(\sigma_x + \sigma_y)\right] \qquad \text{Eq. 5.12}$$

by replacing E with 3μ and ε with $\dot{\varepsilon}$. Note that since $\dot{\varepsilon}_y = \dot{\varepsilon}_z$, an additional equation is required for solving the normal stresses. We use the following constraint:

$$p = \frac{\sigma_x + \sigma_y + \sigma_z}{3} = 0 \qquad \text{Eq. 5.13}$$

Eq. 5.13 describes the constant volume condition, because dilation is linearly proportional to the applied hydrostatic pressure p. Finally, the normal stresses in the three principal directions are solved in terms of viscosity μ and normal strain rate $\dot{\varepsilon}_x$:

$$\sigma_x = 2\mu\dot{\varepsilon}_x \qquad \text{Eq. 5.14}$$

$$\sigma_y = \sigma_z = -\mu\dot{\varepsilon}_x \qquad \text{Eq. 5.15}$$

Therefore, Eq. 5.8 can be rewritten as:

$$\dot{U}_\mu = \frac{3}{2}V\mu\dot{\varepsilon}_x{}^2 = \frac{3}{2}V\mu\left(\frac{d\varepsilon_x}{d\kappa}\frac{d\kappa}{dt}\right)^2 \qquad \text{Eq. 5.16}$$

Since energy is assumed to fully dissipate, an equation of motion can be derived by equating $\dot{W}_\gamma$ to $\dot{U}_\mu$:

$$\frac{d\kappa}{dt} = \frac{2\gamma_{cc}}{3V\mu}\left(\frac{d\varepsilon_x}{d\kappa}\right)^{-2}\frac{dA}{d\kappa} \qquad \text{Eq. 5.17}$$

The κ versus τ relationship described by Eq. 5.17 is not a simple exponential decay because of the right hand side of that differential equation is not linear in κ. In addition, γ_{cc} has the effect of expediting the rounding process, whereas μ provides cells the resistance to shape changes.

Figure 5.7 shows a plot of κ versus annealing τ, with initial value $\kappa_0 = 2.3$, as found using three different approaches. The first approach, "3D FE Interior", presents the result of a

FE simulation, in which an 18-faced cell (Figure 4.6a), with 94 triangular sub-faces, is allowed to anneal while surrounded by other similarly compressed cells. The annealing of this polyhedral cell is characterized by curve *a*. In a similar approach, "3D FE Isolated", the same polyhedral cell undergoes the rounding process while suspended in medium, and is represented by curve *d*. In addition to these simulated results, a theoretical relationship is plotted for comparison. Describing the rounding of a comparable isolated, ellipsoidal cell, "3D Ellipsoid Isolated", curve *e* is plotted using Eq. 5.17 with $\kappa_0 = 2.3$.
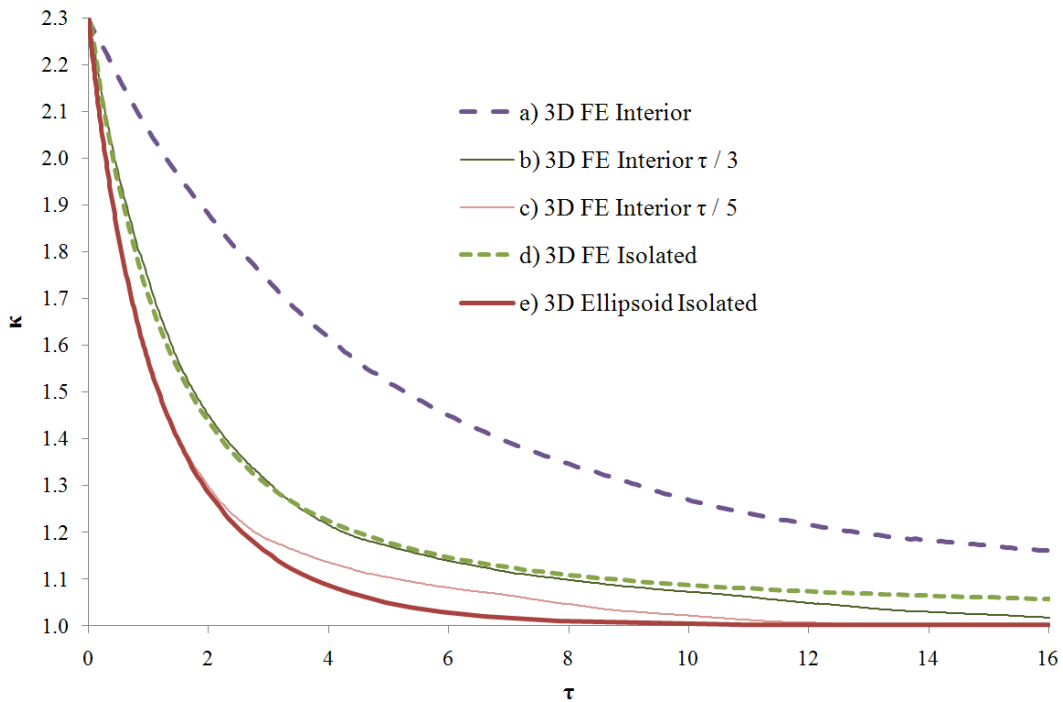
Figure 5.7: Cell aspect ratio versus dimensionless time

Note that all curves eventually go to 1. The gap between dashed curves *a* and *d* is due to the hindering effects of neighboring cells on cell rounding. To determine the appropriate factor to account for this rate difference, a new curve *b* is generated by adjusting the τ axis of curve *a* until an overlap is achieved with curve *d*. With this method, the present study finds that the additional geometric restriction imposed by the presence of neighbors slows down the annealing process of an interior polyhedral cell by a factor of 3.

Further, comparing curves *a*, *d* and *e* reveals that the rounding of FE polyhedral cells occurs at a slower rate than that of theoretical oblate spheroids. This rate difference can be attributed to the extra geometric constraints arisen from the planar sub-surfaces of polyhedra. To investigate the combined impeding effects of both cell neighbors and polyhedral geometries, another new curve *c* is produced by scaling the τ axis of curve *a* to match curve *e*. With a factor of 5, the simulated rounding of an interior polyhedral cell in aggregate corresponds reasonably well with the decay rate of Eq. 5.17. As will be seen later, this factor allows us to compare the results of the parallel plate simulations in this study to the theoretical predictions of Eq. 5.17.

In addition to the two geometric impositions discussed, including cell neighbors and planar sub-surfaces, the annealing rate is affected by the ratio between γ_{cc} and μ as indicated by Eq. 5.17. Figure 5.8 shows the κ versus annealing *t* curves as found using Eq. 5.17 with $\kappa_0 = 1.6$ and γ_{cc}/μ varying from 1 to 5 (black lines). The actual elapsed time *t* is used here instead of the dimensionless time τ, because τ standardizes the ratio between γ_{cc} and μ to a constant value.
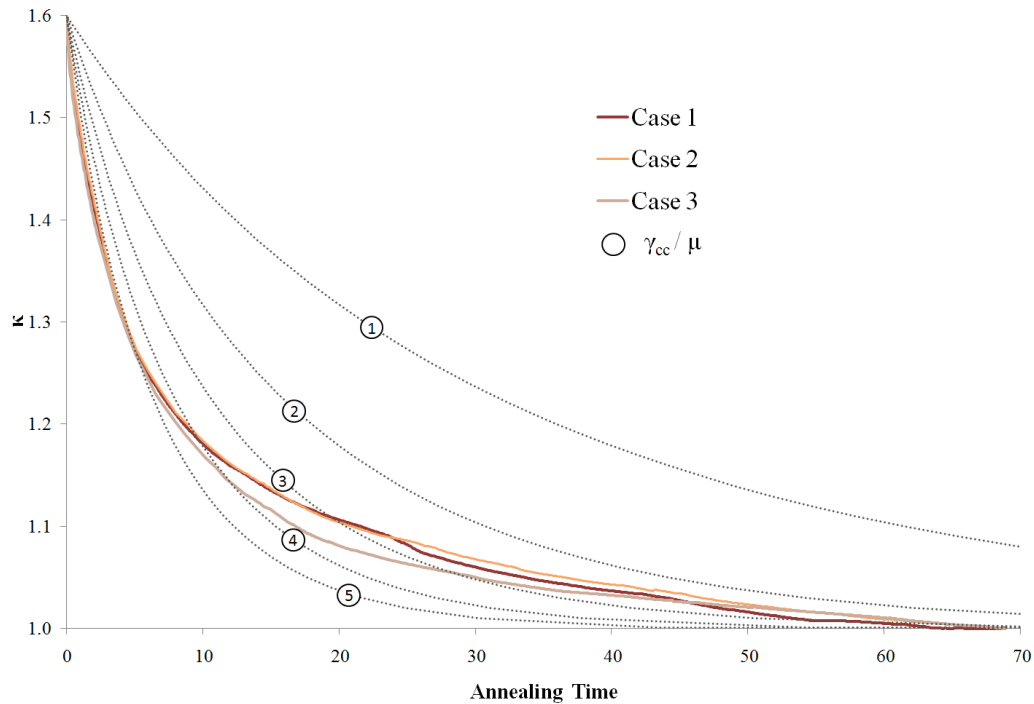

Figure 5.8: Cell aspect ratio versus actual elapsed time

Figure 5.8 shows that a compressed cell returns to its original, spherical shape at a faster rate with a larger γ_{cc}/μ value. This family of theoretical curves is useful, because it enables the evaluation of γ_{cc}/μ ratios from simulated or experimental results. For example, if we superimpose the interior κ_1 curves from this study ($\gamma_{cc}/\mu = 5$) on Figure 5.8 (coloured lines), we observe the initial annealing process to be in good agreement with the $\gamma_{cc}/\mu = 5$ curve. Note that, to match the theoretical predictions of Eq. 5.17, the simulated curves have been shifted down so that $\kappa \to 1$ as $t \to \infty$. In addition, adjustments for volume and the combined effects of cell neighbors and polyhedral geometries have been made to the t axis.

However, the rounding mechanism gradually slows down. This reduced rate is due to the fact that the cell aggregate in this study is held at a fixed compression level. Therefore, for similar parallel plate compression experiments, the ratio between γ_{cc} and μ can be inferred from the annealing rate immediately after compression.

5.2 Correlation of Shape between 2D Cross Sections and 3D Cells

As mentioned, experimental data can be collected more easily if the geometric properties of 2D cross sections can be used to estimate 3D cell shapes. Therefore, we examine the FE meshes to evaluate their correlation. Figure 5.9 combines the interior κ_1 versus annealing τ curves for the three simulation cases, and overlays the 2D interior κ as averaged from 108 parallel cross sections (36 samples from each simulation case) for comparison. The error bars are included to indicate the range of one standard deviation.

For annealing $\tau = 0$ and 140, Figure 5.9 also includes the plan view of the mesh showing the orientation of each cell as a blue line segment. Recall that cell orientation is defined by the direction of eigenvector of $\boldsymbol{I'}_{cell}$ corresponding the largest principal moment of inertia (refer to Section 4.1.4). Figure 5.10 presents the same graph with information from the radial cross sections. Here only the interior cell groups are examined as the κ values for the plate and medium groups do not show much consistency.
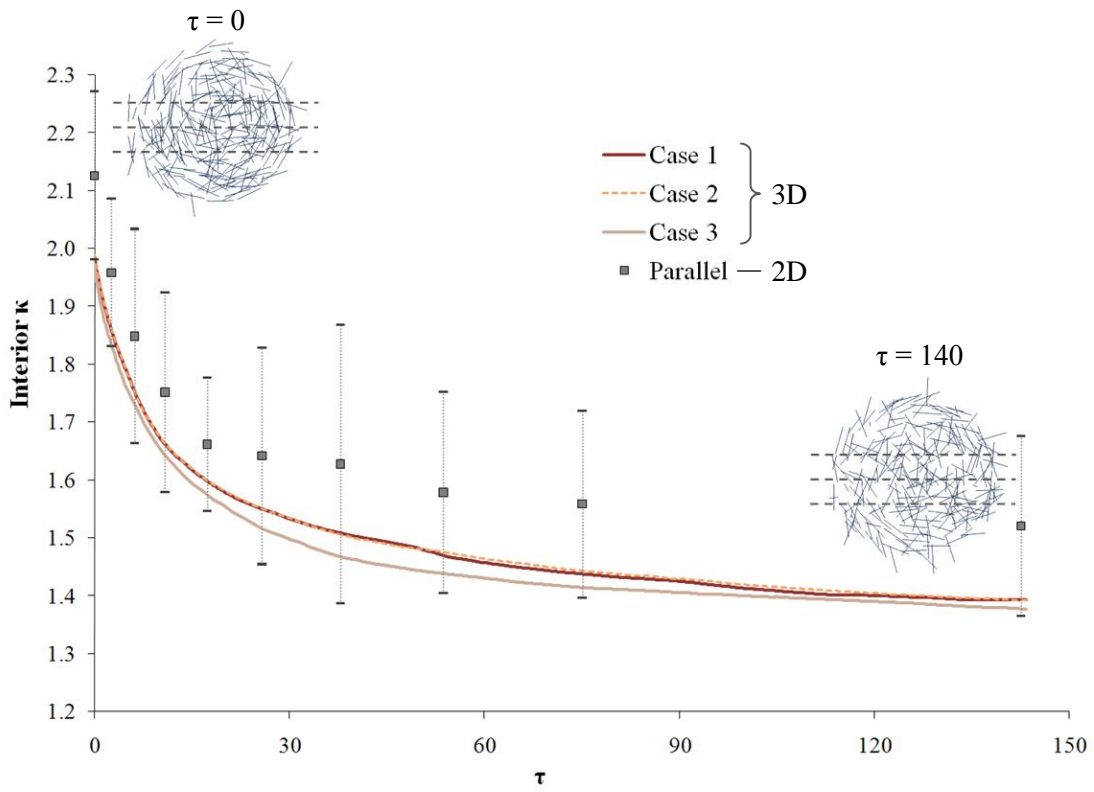
**Figure 5.9: 3D interior κ_1 and 2D interior κ averaged from parallel cross sections**
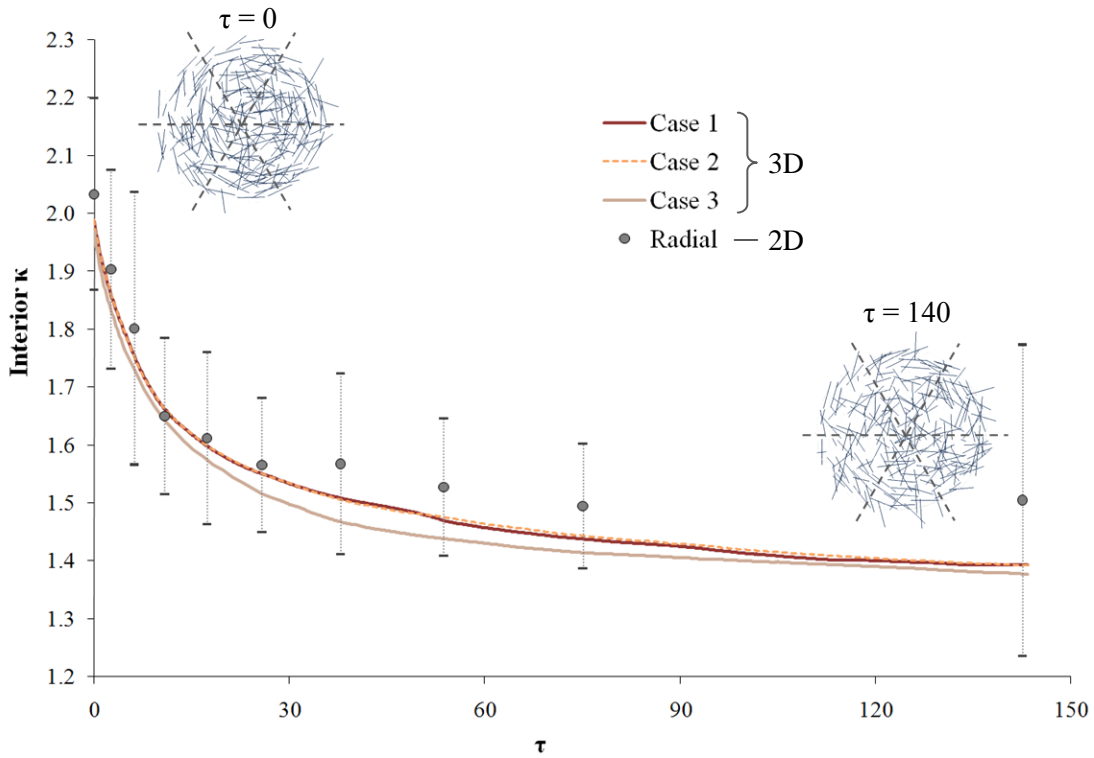
Figure 5.10: 3D interior κ_1 and 2D interior κ averaged from radial cross sections

Using the "equivalent ellipse" method to determine the average anisotropy of 3D aggregates, with 2D cross sections, results in overestimation of κ_1. Considerable fluctuations exist within the data sets; however, the process of cell rounding is still demonstrated in the decaying average κ.

Discrepancies with the actual cell shape: (1) are greater for parallel cross section averages, and (2) increase as the cells anneal for both parallel and radial cross section averages. Both results may be explained by observing how cell orientations change as the annealing progresses. Immediately after compression, at annealing $\tau = 0$, the cells appear to surround the mesh center, forming layers of circles. Cutting this mesh in a radial, as opposed to parallel, manner produces cross sections with lower aspect ratios. Upon annealing, at annealing $\tau = 140$, the orientation of cells are more random as cell rearrangements occur. Figure 5.10 shows that radial cross sections provide an adequate representation of the 3D geometry during the initial annealing process, but not after the cells have re-oriented themselves.

To compare with experimental data, we examine the scanning electron micrograph of an amphibian aggregate (Figure 5.11). This image is taken shortly after the aggregate has reached approximately 50% compression (Phillips and Davis 1978). After critical-point drying by standard techniques, the compressed aggregate is broken in a plane perpendicular to its flattened sides to reveal cells shapes in cross-section. The average κ for each location group is manually extracted from the image as illustrated in Figure 5.11, using the "equivalent ellipse" method outlined in Section 4.2.
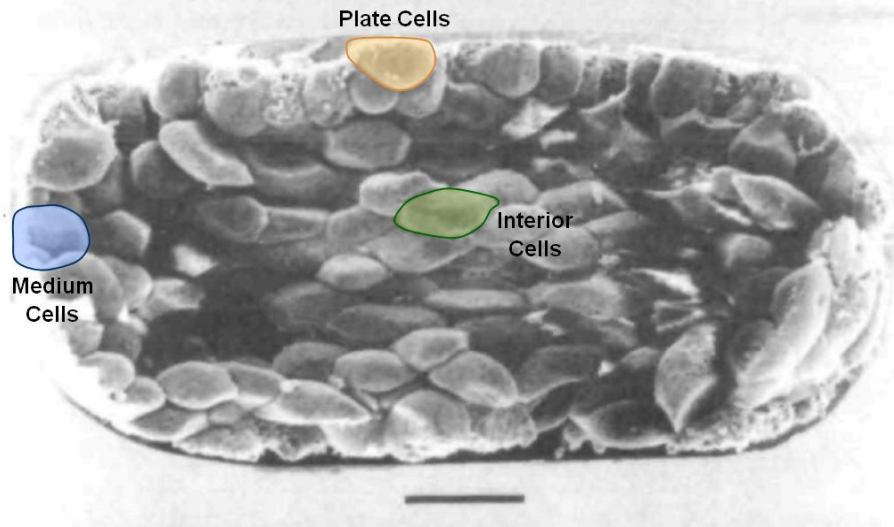
Figure 5.11: Scanning electron micrograph of an aggregate 5 minutes after compression

These extracted average κ values (Table 5.1) are plotted in Figure 5.12 with the average κ_1 versus τ curves for Case 1, in the region immediately after compression.

Table 5.1: Extracted average κ values of the scanning electron micrograph

Type	No. of Cells	Avg. κ
Interior	47	1.86
Plate	16	1.73
Medium	18	1.53
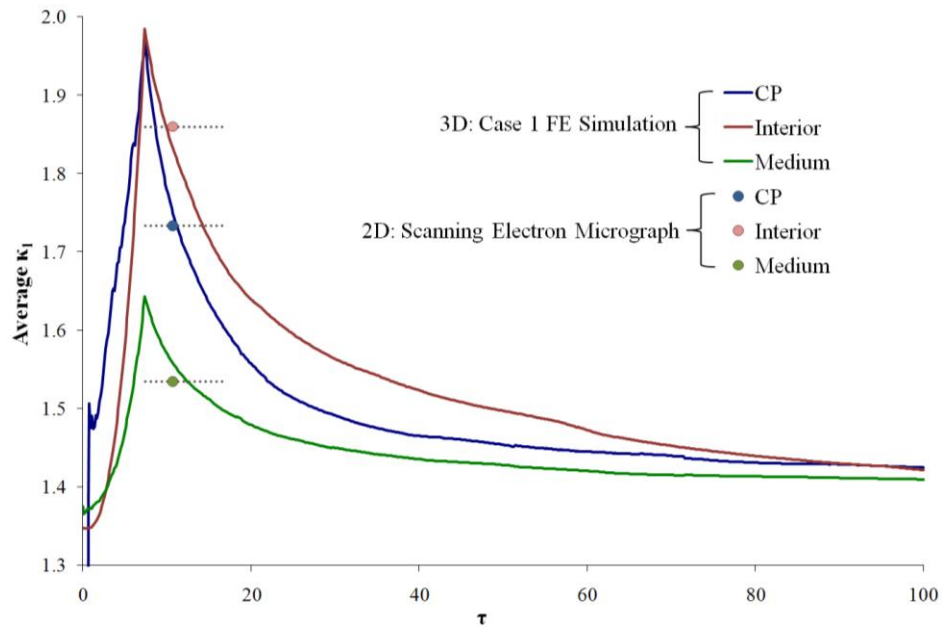
Figure 5.12: Average κ_1 history for Case 1 and average κ values from the scanning electron micrograph

61

Figure 5.12 shows that the average anisotropy of one group with respect to another is in the correct ratio. The absolute values also compare very well. This result demonstrates adequate cell rounding mechanisms of the FE model.

Based on the above, we learned that the time immediately after compression is an important period for analyzing data from parallel compression experiments. During this time, the theoretical equation developed in Section 5.1.2 can be used to interpret the values of γ_{cc} and μ based on the rate of interior cell rounding. In addition, this rate of change in cell shape can be adequately inferred from a set of radial cross sections gathered during the same time. In laboratories these cross sections can be obtained via rotating confocal microscopes. With these two findings, the present study provides a simple method for evaluating the interfacial tension of aggregated cells, which has not been previously achieved.

6 Conclusions and Future Work

Enhancements made to a previous cell rearrangement algorithm allowed the new finite element model developed here to realistically replicate embryonic cell movements and cell shape histories.

The simulations show that the shape of cells in contact with the medium or the compression plates is dominated by their respective medium or plate surface tensions. Medium cells anneal at a slower rate than the interior cells because they are confined to the mass surface. The movement of the plate cells is greatly restricted when the medium surface tension is greater than the plate surface tension. As a result, the plate cells remain significantly compressed.

In contrast, the rounding of interior cells is governed by the ratio between the interfacial tension and cell viscosity. This ratio can be calculated from the cell shape history with the theoretical equation developed in this study (Eq. 5.17). In addition, the study finds that the cell shape history of interior cells can be inferred adequately from a set of radial cross sections. A basis is thus provided for estimating cell-cell interfacial tensions from cell shape histories.

Future work might include validating the finite element simulations by comparison with more experimental data, implementing the Case 4 cell rearrangement algorithm, and analyzing the surface cells in more detail. For instance, the orientation of cells suggests that examining cell shape with respect to a polar coordinate system may provide additional insights. In addition, the reaction forces on the compression plates can also be correlated with cell shape histories.

References

Alberts, B., et al. *Essential cell biology.* 2nd Ed. New York: Garland Science, 2004.

Bausch, A. R., F. Ziemann, A. A. Boulbitch, K. Jacobson, and E. Sackmann. "Local measurements of viscoelastic parameters of adherent cell surfaces by magnetic bead microrheometry." *Biophys. J.* 75 (1998): 2038-2049.

Bausch, A. R., W. Moller, and E. Sackmann. "Measurement of local viscoelasticity and forces in living cells by magnetic tweezers." *Biophysical Journal* 76 (1999): 573-579.

Beysens, D. A., G. Forgacs, and J. A. Glazier. "Cell sorting is analogous to phase ordering in fluids." *PNAS* 97, no. 17 (2000): 9467-9471.

Bodenstein, L. "A dynamic simulation model of tissue growth and cell patterning." *Cell Differentiation* 19 (1986): 19-33.

Brodland, G. W. "Computational modeling of cell sorting, tissue engulfment, and related phenomena: A review." *Appl. Mech. Rev.* 57, no. 1 (2004): 47-76.

Brodland, G. W. "New information from cell aggregate compression tests and its implications for theories of cell sorting." *Biorheology* 40 (2003): 273-277.

Brodland, G. W. "The differential interfacial tension hypothesis (DITH): A comprehensive theory for the self-rearrangement of embryonic cells and tissues." *ASME* 124 (2002): 188-197.

Brodland, G. W., and C. J. Wiebe. "Mechanical effects of cell anisotropy on epithelia." *Computer Methods in Biomech. and Biomed. Eng.* 7, no. 2 (2004): 91-99.

Brodland, G. W., D. Viens, and J. H. Veldhuis. "A new cell-based FE model for the mechanics of embryonic epithelia." *Computer Methods in Biomechanics and Biomedical Engineering* 10, no. 2 (2007): 121-128.

Brodland, G. W., J. Yang, and J. H. Veldhuis. "Computational models reveal that cell-cell interactions are different in 2D than 3D." *Joint WCCM/ECCOMAS Congress.* Venice: Int. Center for Numerical Methods in Eng., 2008.

Chen, C. S., J. L. Alonso, E. Ostuni, G. M. Whitesides, and D. E. Ingber. "Cell shape provides global control of focal adhesion assembly." *Biochemical and Biophysical Research Communications* 307 (2003): 355-361.

Chen, H. H., and G. W. Brodland. "Cell-level finite element studies of viscous cells in planar aggregates." *ASME J. Biomech. Eng.* 122 (2000): 394-401.

Chicurel, M. E., C. S. Chen, and D. E. Ingber. "Cellular control lies in the balance of forces." *Cell Biology* 10 (1998): 232-239.

Clausi, D. A., and G. W. Brodland. "Mechanical evaluation of theories of neurulation using computer simulations." *Development* 118 (1993): 1013-1023.

Clem, C. J., D. Konig, and J. P. Rigaut. "A three-dimensional dynamic simulation model of epithelial tissue renewal." *Analytical and Quantitative Cytology and Histology* 19 (1997): 174-184.

Costa, K. D., W. J. Hucker, and F. C. P. Yin. "Buckling of actin stress fibers: A new wrinkle in the cytoskeletal tapestry." *Cell Motility and the Cytoskeleton* 52 (2002): 266-274.

Evans, E. A., and A. Yeung. "Apparent viscosity and cortical tension of blood granulocytes determined by micropipet aspiration." *Biophys. J.* 56 (1989): 151-160.

Forgacs, G. "Surface tension and viscoelastic properties of embryonic tissues depend on the cytoskeleton." *Biol. Bull.* 194 (1998): 328-330.

Foty, R. A., and M. S. Steinberg. "The differential adhesion hypothesis: a direct evaluation." *Developmental Biology* 278 (2005): 255-263.

Foty, R. A., C. M. Pfleger, G. Forgacs, and M. S. Steinberg. "Surface tensions of embryonic tissues predict their mutual envelopment." *Development* 122 (1996): 1611-1620.

Foty, R. A., G. Forgacs, C. M. Pfleger, and M. S. Steinberg. "Liquid properties of embryonic tissues: Measurement of interfacial tensions." (Physical Review Letters) 72, no. 12 (1994): 2298-2301.

Fournier, J., D. Lacoste, and E. Raphael. "Fluctuation spectrum of fluid membranes coupled to an elastic meshwork: Jump of the effective surface tension at the mesh size." *Physical Review Letters* 92, no. 1 (2004): 018102-1-4.

Fuchizaki, K., T. Kusaba, and K. Kawasaki. "Computer modelling of three-dimensional cellular pattern growth." *Philosophical Magazine B* 71, no. 3 (1995): 333-357.

Goel, N. S., and C. F. Doggenweiler. "Simulation of cellular compaction and internalization in mammalian embryo development as driven by minimization of surface energy." *Bulletin of Math. Biol.* 48, no. 2 (1986): 167-187.

Gov, N., A. G. Zilman, and S. Safran. "Cytoskeleton confinement and tension of red blood cell membranes." *Physical Review Letters* 90, no. 22 (2003): 228101-1-4.

Graner, F., and J. A. Glazier. "Simulation of biological cell sorting using a two-dimensional extended Potts model." *Physical Review Letters* 69, no. 13 (1992): 2013-2016.

Honda, H., M. Tanemura, and T. Nagai. "A three-dimensional vertex dynamics cell model of space-filling polyhedra simulating cell behavior in a cell aggregate." *J. of Theoretical Biology* 226 (2004): 439-453.

Ingber, D. E., D. Prusty, Z. Sun, H Betensky, and N Wang. "Cell shape, cytoskeletal mechanics, and cell cycle control in angiogenesis." *J. Biomechanics* 28, no. 12 (1995): 1471-1484.

Jockusch, B. M., et al. "The molecular architecture of focal adhesions." *Annu. Rev. Cell Dev. Biol.* 11 (1995): 379-416.

Karcher, H., J. Lammerding, H. Huang, R. T. Lee, R. D. Kamm, and M. R. Kaazempur-Mofrad. "A three-dimensional viscoelastic model for cell deformation with experimental verification." *Biophysical Journal* 85 (2003): 3336-3349.

Ketcham, R. A. "Three-dimensional grain fabric measurements using high-resolution X-ray computed tomography." *J. of Structural Geology* 27 (2005): 1217-1228.

Mathur, A. B., A. M. Collinsworth, W. M. Reichert, W. E. Kraus, and G. A. Truskey. "Endothelial, cardiac muscle and skeletal muscle exhibit different viscous and elastic properties as determined by atomic force microscopy." *J. Biomech.* 34 (2001): 1545-1553.

Mermelstein, C. S., M. I. L. Rebello, L. M. Amaral, and M. L. Costa. "Changes in cell shape, cytoskeletal proteins and adhesion sites of cultured cells after extracellular Ca2+ chelation." *Brazilian J. of Medical and Biological Research* 36 (2003): 1111-1116.

Miller, K. "Method of testing very soft biological tissues in compression." *J. of Biomechanics* 38 (2005): 153-158.

Morgan, F. "Mathematicians, including undergraduates, look at soap bubbles." *The Amer. Math. Monthly* 101, no. 4 (1994): 343-351.

Morris, C. E., and U. Homann. "Cell surface area regulation and membrane tension." *J. Membrane Biol.* 179 (2001): 79-102.

Olsen, K. B., R. Nigbor, and T. Konno. "3D viscoelastic wave propagation in the Upper Borrego Valley, California, constrained by borehole and surface area data." *Bulletin of the Seismological Society of America* 90, no. 1 (2000): 134-150.

Palsson, E. "A three-dimensional model of cell movement in multicellular systems." *Future Generation Computer Systems* 17 (2001): 835-853.

Petersen, N. O., W. B McConnaughey, and E. L. Elson. "Dependence of locally measured cellular deformability on position on the cell temperature and cytochalasin B." *Proc. Nat. Acad. Sci. USA* 79 (1982): 5327-5331.

Phillips, H. M., and G. S. Davis. "Liquid-tissue mechanics in amphibian gastrulation: Germ-layer assembly in Rana Pipiens." *Amer. Zool.* 18 (1978): 81-93.

Phillips, H. M., and M. S. Steinberg. "Embryonic tissues as elasticoviscous liquids." *J. Cell Sci.* 30 (1978): 1-20.

Phillips, H. M., and M. S. Steinberg. "Equilibrium measurements of embryonic chick cell adhesiveness, I. shape equilibrium in centrifugal fields." *Proceedings of the National Academy of Sciences of the United States of America* 64, no. 1 (1969): 121-127.

Sato, M., D. P. Theret, L. T. Wheeler, N. Ohshima, and R. M. Nerem. "Application of the micropipette technique to the measurement of cultured porcine aortic endothelial cell viscoelastic properties." *J. Biomech. Eng.* 112 (1990): 263-268.

Schaller, G., and M. Mayer-Hermann. "Multicellular tumor spheroid in an off-lattice Voronoi-Delaunay cell model." *Physical Review E* 71 (2005): 051910.

Selby, S. M., ed. *Standard Mathematical Tables, 14th ed.* Cleveland, Ohio: The Chemical Rubber Co., 1965.

Steinberg, M. S. *Dynamical phenomena at interfaces, surfaces and membranes.* Edited by D. Beysens, N. Boccara and G. Forgacs. Commack, NY: Nova Science Publishers, 1993.

Taylor, J. E. "The structure of singularities in soap-bubble-like and soap-film-like minimal surfaces." *The Annals of Math., 2nd Series* 103, no. 3 (1976): 489-539.

Théry, Manuel, Victor Racine, Anne Pepin, Matthieu Piel, and Yong, Sibarita, Jean-Baptiste, Bornens, Michel Chen. "The extracelluar matrix guides the orientation of the cell division axis." *Nature Cell Biology* 7 (October 2005): 947-953.

Thoumine, O., and A. Ott. "Time scale dependent viscoelastic and contractile regimes in fibroblasts probed by microplate manipulation." *Journal of Cell Science* 110 (1997): 2109-2116.

Tonon, F. "Explicit exact formulas for the 3-D tetrahedron inertia tensor in terms of its vertex coordinates." *J. of Math. and Statistics 1* 1 (2004): 8-11.

Umeda, T., and K. Inouye. "Cell sorting by differential cell motility: a model for pattern formation in Dictyostelium." *J. of Theoretical Biology* 226 (2004): 215-224.

Viens, D., and G. W. Brodland. "A three-dimensional finite element model for the mechanics of cell-cell interactions." *J. of Biomechanical Eng.* 129 (2007): 651-657.

Watson, P. A. "Function follows form: generation of intracellular signals by cell deformation." *The FASEB Journal*, 1991: 2013-2019.

Zhang, Z., M. A. Ferenczi, A. C. Lush, and C. R. Thomas. "A novel micromanipulation technique for measuring the bursting strength of single mammalian cells." *Appl. Microbiol. Biotechnol.* 36 (1991): 208-210.